Pontifícia Universidade Católica
do Rio de Janeiro

Gustavo Alejandro Loachamin Ordonez

Amplitude analysis of the $D_s^+ \to K^-K^+K^+$ decay using the LHCb run 2 data

Dissertação de Mestrado

Dissertation presented to the Programa de Pós-Graduação em Física of PUC-Rio in partial fulfillment of the requirements for the degree of Mestre em Física.

Advisor: Profa. Carla Göbel Burlamaqui de Mello

Rio de Janeiro
March 2023

Pontifícia Universidade Católica
do Rio de Janeiro

Gustavo Alejandro Loachamin Ordonez

Amplitude analysis of the $D_s^+ \to K^-K^+K^+$ decay using the LHCb run 2 data

Dissertation presented to the Programa de Pós-graduação em Física of PUC-Rio in partial fulfillment of the requirements for the degree of Mestre em Física. Approved by the Examination Committee:

Profa. Carla Göbel Burlamaqui de Mello
Advisor
Departamento de Fisica – PUC-Rio

Prof. Alvaro Gomes dos Santos Neto
UnB

Prof. Antonio Vilela Pereira
UERJ

Rio de Janeiro, March 10th, 2023

Gustavo Alejandro Loachamin Ordonez

The author obtained the degree of Bachelor of Science in Honours Physics with distinction in May 2020 from the University of British Columbia UBC (Vancouver, Canada)

Bibliographic data

Loachamin Ordonez, Gustavo Alejandro

Amplitude analysis of the $D_s^+ \to K^-K^+K^+$ decay using the LHCb run 2 data / Gustavo Alejandro Loachamin Ordonez; advisor: Carla Göbel Burlamaqui de Mello. – 2023.

87 f: il. color. ; 30 cm

Dissertação (mestrado) - Pontifícia Universidade Católica do Rio de Janeiro, Departamento de Fisica, 2023.

Inclui bibliografia

1. Fisica – Teses. 2. Charme – Teses. 3. Analise de amplitudes. 4. LHCb. 5. Decaimento. 6. Física de Partículas. 7. Modelo Isobarico. 8. QMIPWA. I. Göbel Burlamaqui de Mello, Carla. II. Pontifícia Universidade Católica do Rio de Janeiro. Departamento de Fisica. III. Título.

CDD: 620.11

To the people and organizations that believe in me,
during my whole career.

Acknowledgments

This study was financed in part by the Coordenação de Aperfeiçoamento de Pessoal de Nível Superior-Brasil (CAPES)-Finance Code 001.

Firstly, I would like to greatly show my gratitude to my dissertation supervisor, professor Carla Göbel, not only for the advice and corrections provided to this research project but also for the help and kindness she offered me during my graduate studies. Her help was invaluable academically and also in my non-academic life. She was the most patient and understanding person I have ever met and who gave me most support and advice during my time in Brazil, especially during the difficult times. I am aware that without Carla's help I would have not finished my master degree. Thank you very much Carla for everything, including letting me be part of your research group. I hope that we meet again in the future.

I also would like to thank professors Alberto dos Reis, Sandra Amato and Erica Polycarpo for their suggestions and help in the research project. Also, I extend my gratitude to all the people in the CharmRio group for their help and advice, especially to Juan Leite who helped me with several technical issues presented in the fitting algorithm scripts.

To Jorge Sgarbi and Maria Eugenia Viancha thank you for your kindness during our time living together. To Giorgio Sgarbi, I am grateful for all the years together and for the help that you offered me. Thank you Giorgio, you were a very important person in my life.

I would like to extend my gratitude to my undergraduate thesis supervisor, professor Michael Hasinoff. I would have not finished my thesis project and I would have not found a graduate student position without his help. Also, I thank all my former professors at UBC for teaching me all the physics I know.

To my closest friends: Jhosmara Barreto, Bryan Llerena, Mirkka Puente and Yuze Zhang, thank you for your love and support during the good and rough times especially Yuze who was the person that help me the most and with whom I shared great adventures and experiences during my time in Vancouver. Also, I am grateful to Kevin Paredes, my dear friend, although it has been a long time since your departure from this world, I still remember the moments we shared and your advice helped me in the roughest moments. I remember you and I will always remember you with love.

Not least important, I would like to thank the Secretaría de Educación Superior, Ciencia, Tecnología e Innovación (SENESCYT) for my undergraduate scholarship.

Finally, I would like to thank life for taking me to so many places during 6 years of adventure, places that made me learn, change and grow as a person.

Abstract

Loachamin Ordonez, Gustavo Alejandro; Göbel Burlamaqui de Mello, Carla (Advisor). **Amplitude analysis of the $D_s^+ \to K^-K^+K^+$ decay using the LHCb run 2 data**. Rio de Janeiro, 2023. 87p. Dissertação de Mestrado – Departamento de Fisica, Pontifícia Universidade Católica do Rio de Janeiro.

Despite of being considered a successful theory in the field of fundamental particles and interactions, the Standard Model is considered incomplete because it still leaves a number of open questions. In order to address some of these, it is necessary to study physical processes such as particle decays. In particular, the decays of heavy hadrons such as D and B mesons can be sensitive to physics beyond the Standard Model, such as new sources of charge-parity violation and new interactions. Nevertheless, at masses at the few GeV range, where perturbative calculations of quantum chromodynamics are limited, phenomenological models are needed to describe their hadronic decays.

In this dissertation, a study of the 3-body decay dynamics of the $D_s^+ \to K^-K^+K^+$ channel is presented for the first time and uses two phenomenological approaches to describe the decay amplitude: the Isobar Model and the Quasi-Model Independent Partial Wave Analysis (QMIPWA). The samples used corresponds to the data collected in Run 2 of the LHCb experiment (between the years 2016-2018) with proton-proton collisions at a center-of-mass energy of 13 TeV.

The analysis is performed after a selection process to reduce background, leading to a final sample of about 100 thousand decays. To perform the amplitude analysis fit to the Dalitz plot of the decay, the remaining background and the efficiency across the Dalitz plot are parametrized. In the case of the Isobar Model, the results obtained show a dominance of the $\phi(1020)$ resonance and a composition of scalar resonances, $f_0(980)$ as the most clear one, being formed as intermediate states, and a small but not negligible contribution of spin-2 resonances. The Isobar Model offers a qualitative description of the decay dynamics but does not provide a good quality fit, even when a variety of possible intermediate states are added to the amplitude model. On the other hand, the QMIPWA as a tool to describe the scalar sector revealed itself difficult for the region of K^-K^+ mass above 1.3 GeV and sensitive to the higher-spin resonances added to the model, making it difficult and less reliable to interpret the results obtained. Even with the limitations found through both models, the analysis presented here represent an important step towards

the understanding of the dynamics of this decay, opening the path to further studies with higher statistics in run 3 of LHCb.

Keywords

Amplitude Analysis; LHCb; Particle Decay; Particle Physics; Isobar Model; QMIPW.

Resumo

Loachamin Ordonez, Gustavo Alejandro; Göbel Burlamaqui de Mello, Carla. **Análise de amplitudes do decaimento $D_s^+ \to K^-K^+K^+$ usando dados do run 2 do LHCb**. Rio de Janeiro, 2023. 87p. Dissertação de Mestrado – Departamento de Fisica, Pontifícia Universidade Católica do Rio de Janeiro.

Apesar de ser considerada uma teoria de sucesso no campo das partículas e interações fundamentais, o Modelo Padrão é considerado incompleto porque ainda deixa uma série de questões em aberto. Para abordar algumas delas, é necessário estudar processos tais como decaimento de partículas. Em particular, os decaimentos de hádrons pesados, como os mésons D e B, podem ser sensíveis à física além do Modelo Padrão, como novas fontes de violação de carga-paridade e novas interações. No entanto, com massas na faixa de poucos GeV, onde os cálculos perturbativos da cromodinâmica quântica são limitados, modelos fenomenológicos são necessários para descrever seus decaimentos hadrônicos. Nesta dissertação, um estudo da dinâmica de decaimento de 3 corpos do canal $D_s^+ \to K^-K^+K^+$ é apresentado pela primeira vez e utiliza duas abordagens fenomenológicas para descrever a amplitude do decaimento: o Modelo Isobárico e a chamada Quasi-Model Independent Partial Wave Analysis (QMIPWA). As amostras utilizadas correspondem aos dados coletados na run 2 do experimento LHCb (entre os anos 2016-2018) com colisões próton-próton a uma energia de centro de massa de 13 TeV. A análise é realizada após um processo de seleção para reduzir o background, levando a uma amostra final com cerca de 100 mil decaimentos. Para realizar a análise de amplitudes no Dalitz plot do decaimento, o background remanescente e a eficiência ao longo do gráfico de Dalitz são parametrizados. No caso em que a amplitude de decaimento é descrita pelo Modelo Isobárico, os resultados obtidos mostram uma dominância da ressonância $\phi(1020)$ e uma composição de ressonâncias escalares, $f_0(980)$ como a mais clara, sendo formada como estados intermediários, e uma pequena mas não desprezível contribuição das ressonâncias de spin-2. O Modelo Isobárico oferece uma descrição qualitativa da dinâmica de decaimento, mas não fornece um ajuste de boa qualidade, mesmo quando uma variedade de possíveis estados intermediários são adicionados ao modelo de amplitude. Por outro lado, o QMIPWA como ferramenta para descrever o setor escalar revelou-se difícil para a região de massa K^-K^+ acima de 1.3 GeV e sensível às ressonâncias de spin mais alto adicionadas ao modelo, tornando difícil e menos confiável a interpretação dos resultados obtidos. Ainda com as limitações encontradas nos dois modelos, a análise apresentada aqui representa um passo

importante para o entendimento da dinâmica deste decaimento, abrindo caminho para estudos com maior estatística no run 3 do LHCb.

Palavras-chave

Analise de amplitudes; LHCb; Decaimento; Física de Partículas; Modelo Isobarico; QMIPWA.

Table of contents

List of figures

List of tables

"Failure is only the opportunity to begin again.
Only this time, more wisely"

Uncle Iroh, .

1
Introduction

The Standard Model of Particle Physics (SM) is considered to be a successful theory because its predictions for particle interactions positively agree with experimental evidence. However, it is also considered an incomplete theory since it fails to provide explanations to some physical phenomena like the nature of dark matter, the barionic-antibarionic asymmetry in the universe, the sources of Charge-Parity (CP) violation and the neutrino masses. Experiments worldwide search for evidence to resolve these issues by performing a huge range of measurements in different subfields of Particle Physics. The CERN complex, for example, hosts some of those experiments using a large accelerator complex and a huge network with several projects involving professionals around the world. The Large Hadron Collider (LHC) is the largest accelerator of the world and the four main experiments of CERN are located around its ring: ATLAS, ALICE, CMS and LHCb. In particular, the LHCb is dedicated to the study of heavy hadrons containing beauty and charm quarks. These projects work in the measurement of CP violation, mixing and the study of the dynamical structure of decays involving these particles (mesons B and D). The decays of these hadrons may be sensitive to observations of new physics. However, the description of the dynamics of these particle decays is challenging since the perturbative methods used for Quantum Chromodynamics (the Standard Model theory of strong interactions) cannot be applied to the theoretically describe the amplitude of these decays. At low energies, many of these decay channels have been widely investigated previously using phenomenological models like the Isobar Model [33]. In this context, we present the amplitude analysis of the $D_s^+ \to K^-K^+K^+$ decay channel using the Isobar model and an attempt to use the Quasi Model Independent Partial Wave Analysis (QMIPWA) in this dissertation. The dynamical structure of the phase space of this decay has not been studied to date. This decay channel is important because the results obtained here might be used in future studies and they might provide more information about hadronic processes at low energies. This dissertation is organized as follows: in chapter 2, a brief description of the Standard Model as a field theory is presented, later we present a description of particle dynamics including the kinematics of a three-body de-

cay, the Dalitz plot formalism and a description of the two phenomenological models used in this work: the Isobar Model and the Quasi-Model Independent Partial Wave Analysis (QMIPWA). Chapter 3 is dedicated to the description of the LHCb experiment with a brief introduction to the LHCb components: the tracking system, calorimeters, particle idetification system, muon chambers and the trigger levels. In chapter 4, a summary of the data selection process is presented: a definition for the kinematic variables measured; the final trigger, pre-selection and selection requirements on the variables used to deal with the combinatorial (association of random tracks) and specifc backgrounds (cross-feed, clone tracks and high asymmetry). This data selection was already performed by Carolina Bolognani in studies of charge-parity CP violation using this decay channel [27]. However, the last requirement to reduce the combinatorial background (BDT requirement) was adjusted in this work to obtain a purity of 90% in the final sample. In chapter 5, the methodology of the fitting procedure is presented along with a description of the background parametrization and the efficiency map construction. Chapter 6 and 7 contain the final results for the fit and the conclusions of this study. The Isobar Model fits show a qualitative description of the phase-space of this decay which is dominated by the $\phi(1020)$ and a S-wave structure (which requires further studies to obtain a satisfactory parametrization). On the other hand, the QMIPWA turned out to be a limited model to describe this decay. The results using these models are reliable up to 1.3 GeV in the invariant mass squared K^-K^+ due to the low data points found beyond this value.

2
Theory

The main goal of this dissertation is to describe the structure of the phase space of the decay $D_s^+ \to K^-K^+K^+$ using the LHCb Run 2 data collected between the years 2016-2018. An attempt for the description of the amplitude (the Lorentz invariant matrix element) of this decay is performed using two phenomenological models: the Isobar Model and the Quasi-Model Independent Partial Wave Analysis (QMIPWA). In this context, it is firstly required a basic understanding of the theoretical foundations of an amplitude analysis. For this reason, a brief description of the theory behind amplitude analysis of particle decays is provided in this chapter including the foundations of the Standard Model, the kinematics of three-body decays and the theoretical description of the phenomenological models used.

2.1
The Standard Model of Particle Physics

The Standard Model (SM) is a theory that successfully provides explanation to the fundamental interactions of nature and to most known phenomena in particle physics [2]. In the SM, the fundamental interactions (except for gravity which is still not included in this theory): electromagnetic, weak and strong are explained as the exchange of Gauge Bosons between the fundamental fermions (and their respective antiparticles [3]). There exist twelve fundamental fermions divided into two equal groups: leptons and quarks. The group of leptons include the electron and two heavier electron-like particles (muon and tau), all of them with their corresponding neutrinos. On the other hand, in the quark sector, there exist three up-type quarks which posses the same charge and three down-type quarks (also with the same charge), all of them with different mass. The fundamental fermions of the SM together with the Gauge Bosons are shown in Fig. 2.1. Mathematically, the SM is a renormalizable non-Abelian (non-commutative) field theory which contains information about the fundamental interactions, has spontaneous symmetry breaking [3], [4] and it is based on the algebra of the group $SU(3) \otimes SU(2)_L \otimes U(1)_Y$. The $SU(3)$ represents the algebra of Quantum Chromodynamics (QCD), the theory of strong interactions, where the mediators of the interaction are eight mass-

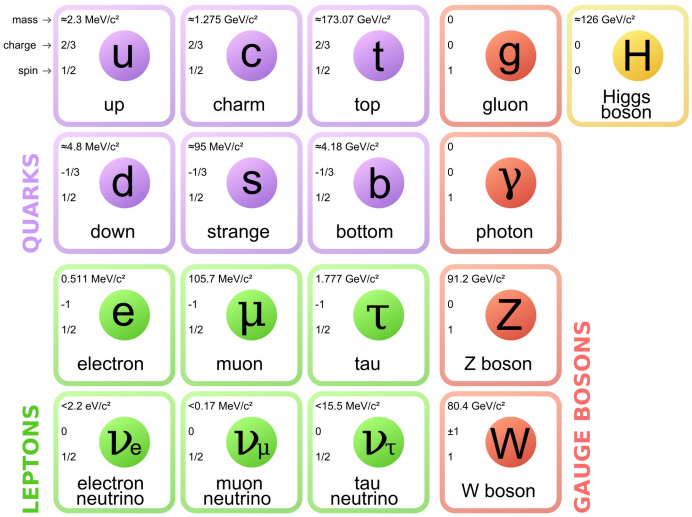

Figure 2.1: Particles of the Standard Model. The twelve fundamental fermions are divided into two groups: leptons and quarks. The Gauge bosons responsible for each fundamental interaction are shown on the right.

less gluons carrying color charge. The strong interaction is responsible for the existence (through the mechanism of confinement) of bound states of quarks called hadrons and there exists two kinds of hadrons: mesons (quark-antiquark bound states) and baryons (triple-quark bound states)[1]. This information is contained in the Lagrangian of QCD, which is given by the expression:

$$\mathcal{L} = -\frac{1}{4}\sum_{A=1}^{8} F^{A\mu\nu}F^{A}_{\mu\nu} + \sum_{j=1}^{n_f}\bar{q}_j(i\not{D} - m_j)q_j \tag{2-1}$$

where $F^{A}_{\mu\nu} = \partial_\mu g^A_\nu - \partial_\nu g^A_\mu - e_S C_{ABC} g^B_\mu g^C_\nu$, g^A_ν are the gluon fields and q_j are the quark fields. The physical allowed vertices of QCD include quark-gluon-quark vertex (represented by the second sum in the Lagrangian) and triple, quartic gluon self-interaction vertices (represented by the first sum in the Lagrangian).

The $SU(2)_L \otimes U(1)_Y$ represents the theory of electroweak interactions. The electroweak Langragian can be split into two components: $\mathcal{L} = \mathcal{L}_{symm} + \mathcal{L}_{Higgs}$ where $\mathcal{L}_{symm}$ is known as the Yang-Mills Lagrangian. The Yang-Mills Lagrangian is given by:

$$\mathcal{L}_{symm} = -\frac{1}{4}\sum_{A=1}^{3} F^{A\mu\nu}F^{A}_{\mu\nu} - \frac{1}{4}B_{\mu\nu}B^{\mu\nu} + \bar{\psi}_L i\gamma^\mu D_\mu \psi_L + \bar{\psi}_R i\gamma^\mu D_\mu \psi_R, \tag{2-2}$$

where $B_{\mu\nu} = \partial_\mu B_\nu - \partial_\nu B_\mu$, $F^{A}_{\mu\nu} = \partial_\mu W^A_\nu - \partial_\nu W^A_\mu - g\epsilon_{ABC} W^B_\mu W^C_\nu$, B_μ is the

[1]Color confinement allows the existence of bound states with higher number of quarks namely tetra and pentaquarks. A constituent quark model was first proposed in [34] and many of these states have already been observed by different collaborations [35] , for example the observation of the $X(3872)$ firstly performed by the Belle collaboration.

gauge field associated with $U(1)_Y$ and W_μ^A are the gauge fields associated with the $SU(2)_L$ generators. The fermion fields are described through the chiral left-hand and right-hand components defined as:

$$\begin{aligned}\psi_{L,R} &= [(1 \mp \gamma_5)/2]\psi \\ \bar{\psi}_{L,R} &= \bar{\psi}[(1 \pm \gamma_5)/2]\end{aligned} \tag{2-3}$$

where ψ are the fermion fields and $P_\pm = (1 \pm \gamma_5)/2$ are the chiral projection operators. The masses of fermions are introduced together with the masses of the mediators through symmetry breaking in the Higgs component of the electroweak Lagrangian. The covariant derivative in Eq. 2-2 can be explicitly written as:

$$D_\mu \psi_{L,R} = [\partial_\mu + ig \sum_{A=1}^{3} t_{L,R}^A W_\mu^A + ig' \frac{1}{2} Y_{L,R} B_\mu]\psi_{L,R} \tag{2-4}$$

where $t_{L,R}^A$ and $\frac{1}{2}Y_{L,R}$ are the generators of the $SU(2)$ and $U(1)$ symmetries respectively. Then, the charged current coupling (the fermion-$W^\pm$-fermion vertex) can be written as:

$$V_{\bar{\psi}\psi W} = g\bar{\psi}\gamma_\mu[(t_L^+/\sqrt{2})(1-\gamma^5)/2 + t_R^+/\sqrt{2})(1+\gamma^5)/2]\psi W_\mu^- + h.c. \tag{2-5}$$

with $t^\pm = t^1 \pm it^2$ and $W^\pm = (W^1 \pm iW^2)/\sqrt{2}$. In the case of the neutral currents:

$$\begin{aligned}A_\mu &= \cos\theta_W B_\mu + \sin\theta_W W_\mu^3 \\ Z_\mu &= -\sin\theta_W B_\mu + \cos\theta_W W_\mu^3,\end{aligned} \tag{2-6}$$

the physical mediators of the electroweak interactions (photon, $W^\pm$ and Z^0) are a combination of the fields coming from the $SU(2)_L$ and $U(1)_Y$. After symmetry breaking of electroweak interactions, the physically allowed vertices of the weak interactions including charged mediators ($W^\pm$) involve change of particle type (called flavour) at each of these vertices. On the other hand, the interactions involving neutral-charged mediators: photons and Z^0 do not allow flavour change. The study of flavour changing interactions is called flavour physics.

2.1.1 Flavour physics

From the discussion above, it is clear that strong and electromagnetic interactions are flavour unchanging, meaning that the flavour is conserved

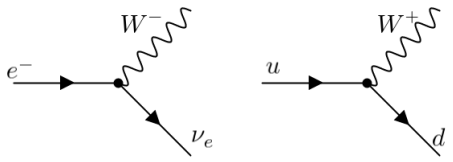

Figure 2.2: Example of vertices allowed in weak interactions.

at each vertex of Feymann diagrams involving these mediators; this is also true for the neutral current (NC) of weak interactions which involve the exchange of Z_0 bosons. On the other hand, the charged current of the weak interaction mediated by the $W^{\pm}$ bosons introduces flavour change at every vertex associated to these mediators as shown in Fig. 2.2. In the case of leptons, there exists only coupling between leptons and their corresponding neutrinos; in addition, the coupling strength is the same for all three generations of leptons (this is known as lepton universality). In the case of quarks, there exists generation change and the coupling strength is not the same for vertices in Feymann diagrams involving different particles due to the difference in quark mass (as mentioned above, all quarks have different mass and only the mass values of the u and d quarks are very close). This mass difference is translated into off-diagonal terms in the mass matrices of the Yukawa Lagrangian. However, these matrices can be diagonalized in such way that we obtain:

$$\mathcal{L}_Y = -\left(1+\frac{H}{v}\right)\{\bar{\boldsymbol{d}}\mathcal{M}_d\boldsymbol{d} + \bar{\boldsymbol{u}}\mathcal{M}_u\boldsymbol{u} + \bar{\boldsymbol{l}}\mathcal{M}_l\boldsymbol{l}\}, \tag{2-7}$$

where the matrices $\mathcal{M}_i$ are diagonal and we can define the mass eigenstates in terms of the weak eigenstates:

$$\begin{aligned} \boldsymbol{d}_L &= \mathbf{S}_d\boldsymbol{d}'_L \qquad \boldsymbol{u}_L = \mathbf{S}_u\boldsymbol{u}'_L \qquad \boldsymbol{l}_L = \mathbf{S}_l\boldsymbol{l}'_L \\ \boldsymbol{d}_R &= \mathbf{S}_d\mathbf{U}_d\boldsymbol{d}'_R \qquad \boldsymbol{u}_R = \mathbf{S}_u\mathbf{U}_u\boldsymbol{u}'_R \qquad \boldsymbol{l}_R = \mathbf{S}_l\mathbf{U}_l\boldsymbol{l}'_R, \end{aligned} \tag{2-8}$$

here $\mathbf{U}_i$ and $\mathbf{S}_i$ are unitary matrices that are used for the diagonalization of the mass matrix. The neutral currents given by $\bar{\boldsymbol{f}}_{L,R}\boldsymbol{f}_{L,R} = \bar{\boldsymbol{f}}'_{L,R}\boldsymbol{f}'_{L,R}$ do not change flavour since this part of the $SU(2)_L \otimes U(1)_Y$ Lagrangian does not change when mass eigenstates are used. However, $\bar{\boldsymbol{u}}'_L\boldsymbol{d}'_L = \bar{\boldsymbol{u}}_L\mathbf{S}_u\mathbf{S}_d^{\dagger}\boldsymbol{d}_L = \bar{\boldsymbol{u}}_L\mathbf{V}^{CKM}\boldsymbol{d}_L$ so a unitary mixing matrix in the quark charged-current sector appears when the Lagrangian is written in terms of the mass eigenstates [16]:

$$\mathcal{L}_{CC} = \frac{g}{2\sqrt{2}}\left\{W_\mu^{\dagger}\left[\sum_{ij}\bar{u}_i\gamma_\mu(1-\gamma_5)\mathrm{V}_{ij}^{CKM}d_j\right] + h.c.\right\} \tag{2-9}$$

where **V** is known as the Cabibbo–Kobayashi–Maskawa (CKM) matrix which is explicitly written as [17]:

$$\mathbf{V}^{CKM} = \begin{pmatrix} V_{ud} & V_{us} & V_{ub} \\ V_{cd} & V_{cs} & V_{cb} \\ V_{td} & V_{ts} & V_{tb} \end{pmatrix} = \begin{pmatrix} 1-\lambda^2/2 & \lambda & A\lambda^3(\rho - i\eta) \\ -\lambda & 1-\lambda^2/2 & A\lambda^2 \\ A\lambda^3(1-\rho-i\eta) & -A\lambda^2 & 1 \end{pmatrix} + \mathcal{O}(\lambda^4), \tag{2-10}$$

the parametrization on the right-hand side is known as the Wolfenstein parametrization [18] with four independent parameters λ, A, ρ, η; since λ is experimentally known to be small, only the first term can be kept from the expansion. Transitions which involve only diagonal terms of the matrix are called *Cabbibo-favoured*, when one off-diagonal term is involved the transition is known as *Cabbibo-suppressed* and if both terms are off-diagonal, the transition is known as *doubly Cabbibo-suppressed*.

2.2 The $D_s \to K^-K^+K^+$ decay

The focus of this work is the description of the *Cabibbo-supressed* decay channel $D_s^+ \to K^-K^+K^+$ which undergoes a transition of the charm quark $c \to s\bar{s}u$ and mainly proceeds in four types of topologies: annhiliation, tree-level with the internal/external emission of a W boson and the penguin diagram. These topologies are shown in Fig. 2.3. The D_s^+ decay amplitude is suppressed with respect to the tree-level diagram which is proportional to $V_{cs}V_{us}^*$ of order $\mathcal{O}(\lambda)$ in Wolfenstein parametrisation given in Eq.2-10.

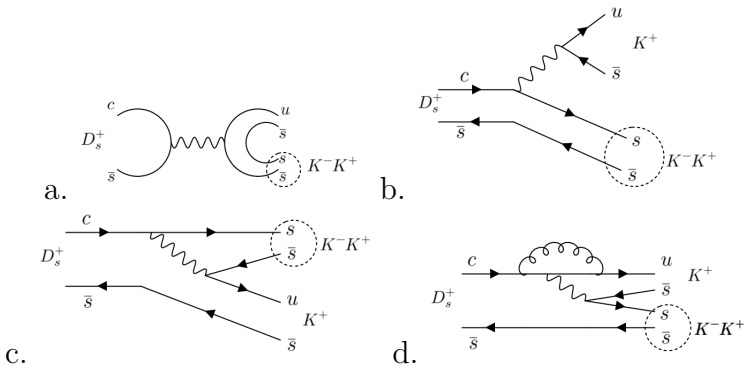

Figure 2.3: Topologies of the $D_s \to K^-K^+K^+$: a. the annhiliation diagram of tree-level order, b. the external and c. internal emission of a W and d. the penguin diagram.

Provided that quarks are always present in bound states, weak interactions involving hadrons are always tangled to strong interactions. For this rea-

son, the description of these processes is generally speaking non-trivial within the SM however, they can still be simplified using different mechanisms.

For example in leptonic decays (like $\pi^- \to \mu\bar{\nu}$), the bound-state effects can be simply reduced to a constant. On the other hand, the description of semi-leptonic decays (like $K^0 \to \pi^+\mu\bar{\nu}$) requires the use of form factors. However in the case of non-leptonic decays, the description is more involved given the complicated structures formed in Feynman diagrams [35]. Therefore, the dynamics of non-leptonic decays cannot be described using first principles. Given that the decay channel studied in this dissertation is non-leptonic, phenomenological models are required in an attempt to provide a description of the amplitude of this decay.

2.2.1 Kinematics of three-body decays

In order to begin with the description of the amplitude of the decay channel $D_s^+ \to K^-K^+K^+$, theoretical foundations on the kinematics of particle decays have to be introduced before presenting the phenomenological models used in this study. Particularly, we talk about the kinematics of three-body decays (one mother, three daughter particles).

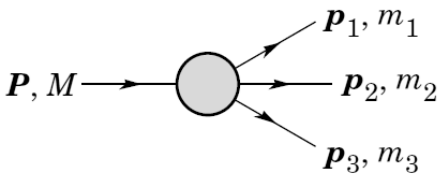

Figure 2.4: Schematic of a three body decay. [24]

The amplitude of a decay is theoretically related to the decay rate for that process. The decay rate is defined as the number of events per unit time of a given decay. In general, particles can decay to an arbitrary number of daughters, provided that energy-momentum conservation is satisfied. For multi-body decays the theoretical expression for the decay rate is given by the following equation:

$$\Gamma \propto \int |\mathcal{M}|^2 \delta^4(P^\mu - \sum_{i=1}^{N} p_i^\mu) \prod_{i=1}^{N} \delta(\mathbf{p}_i^2 - m_i^2) d^4 p_i^\mu, \tag{2-11}$$

where p_i^μ are the four-momenta of the daughter particles involved in the decay, P^μ is the four-momentum of the mother particle and $\mathcal{M}$ is the amplitude which contains the information about the dynamical structure of the decay. The

expression given in Eq. 2-11 is general for any number of daughter particles, and it can be reduced to:

$$\Gamma \propto \int |\mathcal{M}|^2 \delta^4(P^\mu - p_1^\mu - p_2^\mu - p_3^\mu)\delta(\mathbf{p}_1^2 - m_1^2)\delta(\mathbf{p}_2^2 - m_2^2)\delta(\mathbf{p}_3^2 - m_3^2)d^4p_1^\mu d^4p_2^\mu d^4p_3^\mu \tag{2-12}$$

for a three-body decay of the form $M \to P_1P_2P_3$ (this decay is schematically shown in Fig. 2.4; in the case of the decay presented in this dissertation: $D_s^+ \to K^-(P_1)K^+(P_2)K^+(P_3)$). Additionally, the momentum and energy dependence in Eqs. 2-11 and 2-12 can be replaced by a dependence on Lorentz invariant quantities. The Lorentz invariant expressions used in this study are the invariant masses squared which definition is given in Eq. 2-13.

$$\begin{aligned} s_{12} &= (p_1^\mu + p_2^\mu)^2 = (P^\mu - p_3^\mu)^2 \\ s_{13} &= (p_1^\mu + p_3^\mu)^2 = (P^\mu - p_2^\mu)^2 \\ s_{23} &= (p_2^\mu + p_3^\mu)^2 = (P^\mu - p_1^\mu)^2 \end{aligned} \tag{2-13}$$

These invariant masses squared possess many algebraic properties, one that is relevant for this analysis is given below in Eq. 2-14:

$$s_{12} + s_{13} + s_{23} = M^2 + m_1^2 + m_2^2 + m_3^2 \tag{2-14}$$

where M and m_i are the masses of the mother and daughter particles respectively. Replacing all the momentum and energy variables to invariant masses squared reduces the expression in Eq. 2-12 to:

$$\frac{\Gamma}{ds_{12}ds_{13}} = \frac{1}{(2\pi)^3}\frac{1}{32M^3}|\mathcal{M}|^2. \tag{2-15}$$

In Eq. 2-15, it can be seen that the differential decay rate is described by only 2 variables and it is proportional to the square of the amplitude. In general, a three-body decay has twelve degrees of freedom (energy and three-momentum of the daughter particles involved) which can be reduced to 9 given the energy-momentum relations, then they can be reduced to 5 using energy-momentum conservation and provided that the final state particles are scalar (spin-0), a rotational invariance is introduced and the degrees of freedom are reduced to 2. In this study, the variables chosen are s_{12} and s_{13} since intermediate states are expected to appear in the $R \to K^-K^+$ decay channel.

The 2D-phase space described by these two variables is known as a Dalitz plot (DP). Given that the differential decay rate is proportional to the amplitude squared, the density of events in a DP describes the amplitude

of that decay. Therefore, the dynamical structure of a three-body decay can be qualitatively/quantitatively analyzed in a DP. The kinematic limits of the DP are given by the maximum and minimum physical values of the invariant masses squared. To obtain the kinematic limits, we start from the definition of the invariant masses squared given in Eq 2-13 and make some algebraic work in terms of momentum and energy:

$$\begin{aligned} s_{12} &= m_1^2 + m_2^2 + 2p_1^\mu p_{2\mu} \\ s_{12} &= m_1^2 + m_2^2 + 2(E_1E_2 - \mathbf{p}_1 \cdot \mathbf{p}_2) \\ s_{12} &= m_1^2 + m_2^2 + 2(E_1E_2 - |\mathbf{p}_1||\mathbf{p}_2|\cos\theta_{12}), \end{aligned} \tag{2-16}$$

for any given values of energy and momentum the last expression clearly minimizes for $\cos\theta_{12} = 1$ (when particles 1 and 2 travel in the same direction) and maximizes for $\cos\theta_{12} = -1$ (when particles 1 and 2 travel in opposite directions). In this context, we can define a reference frame R_{ij} where $\mathbf{p}_i + \mathbf{p}_j = 0$ for a pair of daughter particles. In the case of the frame R_{12}, the momentum and energy of the daughter particles in terms of the invariant mass s_{12} are given by:

$$\begin{aligned} E_1 = \frac{s_{12} + m_1^2 - m_2^2}{2\sqrt{s_{12}}} \quad E_2 = \frac{s_{12} + m_2^2 - m_1^2}{2\sqrt{s_{12}}} \\ E_3 = \frac{M^2 - s_{12} - m_3^2}{2\sqrt{s_{12}}} \end{aligned} \tag{2-17}$$

and making use of the relation $E_i^2 = \mathbf{p}_i^2 + m_i^2$, we can also find the expressions for the magnitude of the three-momenta of the particles:

$$\begin{aligned} |\mathbf{p}_1| = |\mathbf{p}_2| = \frac{\lambda^{1/2}(s_{12}, m_2^2, m_1^2)}{2\sqrt{s_{12}}} \\ |\mathbf{p}_3| = \frac{\lambda^{1/2}(M^2, s_{12}, m_3^2)}{2\sqrt{s_{12}}} \end{aligned} \tag{2-18}$$

where $\lambda(x, y, z) = x^2 + y^2 + z^2 - 2xy - 2yz - 2xz$ is known as the Källén function [6]. Using these results, we can express the maximum and minimum values of s_{13} in terms of s_{12} in the R_{12} reference frame which provides a boundary for the Dalitz plot:

$$
\begin{aligned}
s_{13} =& m_1^2 + m_3^2 + 2p_1^\mu p_{3\mu} \\
s_{13}^{max/min} =& m_1^2 + m_3^2 + 2(E_1 E_3 \pm |\mathbf{p}_1||\mathbf{p}_3|) \\
s_{13}^{max/min} =& m_1^2 + m_3^2 + \frac{1}{2s_{12}}((s_{12} + m_1^2 - m_2^2)(M^2 - s_{12} - m_3^2) \\
& \pm \lambda^{1/2}(s_{12}, m_2^2, m_1^2)\lambda^{1/2}(M^2, s_{12}, m_3^2)).
\end{aligned} \tag{2-19}
$$

On the other hand, the absolute maximum and minimum values of the invariant masses squared are given by conservation of energy and are shown in the following expression:

$$(m_i + m_j)^2 \leq s_{ij} \leq (M - m_k)^2 \tag{2-20}$$

for $1 \leq i, j, k \leq 3$ and $i \neq j \neq k$. In Fig. 2.5, an example of a Dalitz plot constructed using s_{12} and s_{23} for a given three-body decay is shown. In the decay channel presented in this work, all the daughters possess the same mass so we may construct a "folded Dalitz" plot given that there exist no distinction between particles 2 and 3. The folded Dalitz plot is only filled in the region $s_{13} > s_{12}$ and for data points $s_{12} < s_{13}$, we mirror them in the allowed region so that a point (s_{12}, s_{13}) becomes (s_{13}, s_{12}). The folded DP's are not utilized in this analysis (given that the fitting algorithm cannot deal with this kind of Dalitz plots) however, their use should be employed in further research of this decay channel. In this analysis, only symmetric Dalitz plots are used: DP's in which a pair, (s_{12}, s_{13}) is plotted as (s_{12}, s_{13}) and as (s_{13}, s_{12}), the same case for a pair (s_{13}, s_{12}) and the entire DP phase space is filled (all the phase within the DP boundaries).

2.3 The Isobar Model

As mentioned in the previous sub-section, the description of non-leptonic decays represents a challenge within the Standard Model due to the complicated structure of the strong interactions. For this reason, phenomenological models to describe these decays have to be introduced. A common approach to describe the amplitude of a three-body decay is the Isobar Model. In the Isobar Model, the amplitude of a three-body decay is given by the coherent sum of intermediate states' amplitudes, which appear in the initial two-body intermediate decay $D_s^+ \to RK^+$ and later the resonant state decays into the two final products $R \to K^-K^+$, these intermediate states are known as resonances. This is shown schematically in Fig.2.6.

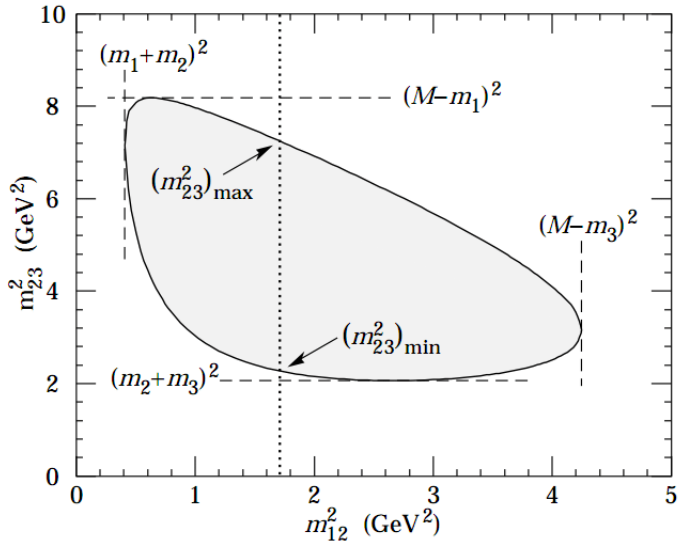

Figure 2.5: Dalitz plot example, the maximum and minimum values of the Dalitz phase space are represented by vertical and horizontal lines. Image taken from [17].

The parent particle may also decay directly into the final products and this non-resonant amplitude (NR) is usually modelled as constant throughout the entire phase space. Therefore, the Lorentz invariant matrix element is given by:

$$\mathcal{M}(s_{12}, s_{13}) = c_{NR} + \sum_i c_i A_i(s_{12}, s_{13}) \tag{2-21}$$

where $c_i = a_i e^{i\phi_i}$ are complex coefficients that are to be determined in the amplitude analysis. One of the coefficients, c_i, should remain fixed in the fit (amplitude and phase) to establish a reference for the rest of the coefficients. Furthermore, the amplitudes A_i are given by the product of forms factors called Blatt-Weisskopf factors (which accounts for the hadronic barrier effects and depends on the spin of the resonance), an angular distribution (which accounts for angular momentum distribution) and a lineshape representing the propagator of the resonant. All of these components can be written in terms of the DP variables which are usually chosen to be the invariant squared masses where the resonances appear. In the case of the decay channel $D^+ \to K^-(1)K^+(2)K^+(3)$, resonances should appear in the two-body decay channel $R \to K^-K^+$ [7] which correspond to the Dalitz plot variables s_{12} and s_{13} since the decay is symmetric. The expected contribution to the amplitude

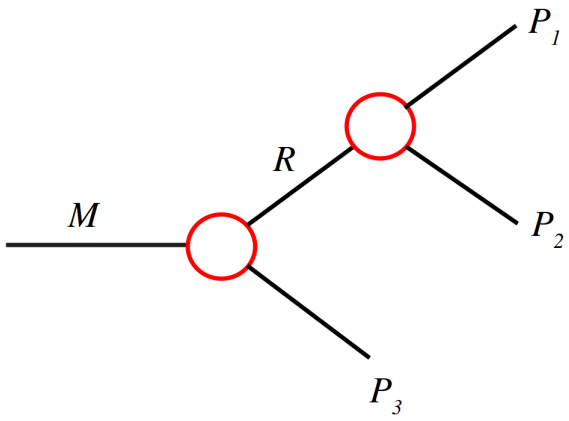

Figure 2.6: Schematics of three-body decay proceeding through an intermediate state.

given by each resonant state is shown in the expression below:

$$A_i(s_{12}, s_{13}) = \mathrm{R}(s_{12}) \times \mathrm{T}(\mathbf{p}, \mathbf{q}) \times F(|\mathbf{p}| r^P_{\mathrm{BW}}) \times F(|\mathbf{q}| r^R_{\mathrm{BW}}), \qquad (2\text{-}22)$$

the amplitude is symmetric under $s_{12} \to s_{13}$ due to Bose-Einstein symmetrization which implies that $A_i(s_{12}, s_{13}) = A_i(s_{13}, s_{12})$ In Eq. 2-22, $\mathbf{q}$, $\mathbf{p}$ are the 3-momenta of one of the resonant decay products and of the spectator particle (the particle that is not involved in the channel associated to the resonant) respectively, both of them calculated in the rest frame of the resonant. $\mathrm{R}(s_{12})$ is the lineshape propagator that represents the phenomenological properties of the resonance. $\mathrm{T}(\mathbf{p}, \mathbf{q})$ is the angular distribution which depends on the spin of the resonance and it is given by the Zemach tensor formalism [9] and $F(z)$ are the Blatt-Weisskopf factors [10] which account for the vertex effects.

2.3.1 Blatt-Weisskopf factors

The Blatt-Weisskopf barrier penetration form factors account for the finite extent of quark bound states which limits the value of the angular momentum. These factors are parametrized by the quantity $z = |\mathbf{p}|r$ where r is the effective radius of the barrier. In the case of the parent decay, $r^P_{BW} = 5.0$ GeV^{-1} and for the resonance $r^R_{BW} = 1.5$ GeV^{-1}. The mathematical expressions of these factors depend on the spin of the resonance, the equations for resonances up to spin 2 are given below (in the amplitude analysis presented

in this study, only resonant states up to spin 2 are used in the fitting models):

$$
\begin{aligned}
F(z)_{J=0} &= 1 \\
F(z)_{J=1} &= \sqrt{\frac{1}{1+z^2}} \\
F(z)_{J=2} &= \sqrt{\frac{1}{z^4+3z^2+9}}
\end{aligned}
\tag{2-23}
$$

2.3.2 Angular distributions

The angular distributions represent the effects of angular momentum in the decays and are given by the Zemach tensor formalism [9]. Mathematically, these distributions depend on the angle between the spectator particle and one of the products of the resonance decay in the rest frame of the resonance (the angle θ_{13} in our case). These distributions depend on the spin of the particle and are summarized in Table 2.1 (up to resonances of spin 2).

Resonance Spin	Angular Distribution
0	1
1	$-2\mathbf{p}\cdot\mathbf{q}$
2	$\frac{4}{3}[3(\mathbf{p}\cdot\mathbf{q})^2 - (\lvert\mathbf{p}\rvert\lvert\mathbf{q}\rvert)^2]$

Table 2.1: Angular distributions used in the resonance amplitudes given by the Zemach tensor formalism

2.3.3 Lineshapes

The lineshapes contain the phenomenological characteristics of the resonances. The most typical lineshape used to describe resonant states is the Breit-Wigner distribution which is based on the study of the behavior of unstable particles [8]. The non-relavistic Breit-Wigner distribution is given by the equation:

$$
\mathrm{BW}(E) \propto \frac{1}{\Gamma^2/4 + (E-E_0)^2} \tag{2-24}
$$

In the case of relativistic particles, the relativistic Breit-Wigner is used; this lineshape is given by the following expression [11]:

$$\mathrm{RBW}(m) = \frac{1}{(m_0^2 - m^2) - im_0\Gamma(m)}, \tag{2-25}$$

where m_0 is the nominal mass of the resonance, $m^2 = s_{ij}$ is the invariant mass squared of the resonance decaying to particles i and j, and $\Gamma(m)$ is the mass-dependent width of the resonance given by:

$$\Gamma(m) = \Gamma_0 \left(\frac{|\mathbf{q}|}{|\mathbf{q}_0|}\right)^{(2L+1)} \left(\frac{m_0}{m}\right) \frac{F(z)}{F(z_0)}. \tag{2-26}$$

Another lineshape commonly used in the analysis of resonances close the to threshold of the phase space of a two-body particle decay is the Flatté distribution. This lineshape was first introduced to describe the a0(980) scalar resonance in the $\pi\eta$ invariant mass distribution near the $K\bar{K}$ threshold [12]. In this analysis, the Flatté distribution is used to describe the scalar resonance f0(980). The Flatté distribution is a modified version of the relativistic Breit-Wigner distribution and it is given by the following expresion:

$$Fl(m) = \frac{1}{m_0^2 - m^2 - im_0(g_{\pi\pi}^2\rho_{\pi\pi} + g_{KK}^2\rho_{KK})}. \tag{2-27}$$

The constants $g_{\pi\pi} = 0.165$ GeV and $g_{KK} = 4.21 g_{\pi\pi}$ [13] represent the couplings of the f0(980) scalar to the final states $\pi^+\pi^-$ and K^+K^- respectively. The factors ρ are given by the following expresions:

$$\rho_{\pi\pi} = \frac{2}{3}\sqrt{1 - \frac{4m_{\pi^\pm}^2}{m^2}} + \frac{1}{3}\sqrt{1 - \frac{4m_{\pi^0}^2}{m^2}} \tag{2-28}$$

$$\rho_{KK} = \frac{1}{2}\sqrt{1 - \frac{4m_{K^\pm}^2}{m^2}} + \frac{1}{2}\sqrt{1 - \frac{4m_{K^0}^2}{m^2}} \tag{2-29}$$

$$. \tag{2-30}$$

In Fig. A.1, the DP's constructed using simulated samples with the Isobar model are presented. These plots show the phase space of the $D_s^+ \to K^-K^+K^+$ decay, each one with a single resonant state allowed in the two-body decay channel $R \to K^-K^+$. The $\phi(1020)$ is well localized due to its small width value and it presents a node characteristic of spin-1 resonances. The spin-1 $\rho(1450)$ also presents a node and spreads over the entire phase-space of the decay due to its relatively large width value. The spin-0 resonances, also known as scalar, spread over the entire the phase-space of the decay except for the $f_0(980)$ which is located and spreads close to the threshold. Finally, the two

spin-2 resonances present two nodes.

2.4 Quasi Model Independent Partial Wave Analysis (QMIPWA)

The parametrization of the S-wave is a complicated task which is sometimes not well performed using the Isobar Model due to the difficulty presented when trying to separate the lineshapes of resonances that are not well localized (usually scalar resonances with large width values). The QMIPWA is an alternative method to obtain a quasi-model independent parametrization of the S-wave (scalar resonances) of a given decay while still describing the higher-spin waves through the Isobar Model. In the QMIPWA, the S-wave is modelled in different bins and later a cubic spline is performed to obtain the S-wave at each point of the mass spectrum. The QMIPWA may provide a description for other resonances that are not visible in a decay phase-space. This technique was first used in [30]. In this quasi-model-independent, the amplitudes A_i for high-spin resonances are given by Eq. 2-22, then the final amplitude is given by:

$$A(s_{12}, s_{13}) = A_{S-wave} + \sum_{spin>0} c_i A_i(s_{12}, s_{13}) \tag{2-31}$$

where the c_i coefficients are to be found in the fit and the amplitude of the S-wave is parametrized at each bin of the K^+K^- invariant mass spectrum by the expression $A^k_{S-wave}(m_{K^+K^-}) = a^k e^{i\phi^k}$. The S-wave is Bose-symmetrized so in any given bins k in m_{12} and l in m_{13}, the amplitude of the S-wave is given by $A^{k,l}_{S-wave}(s_{12}, s_{13}) = A^k_{S-wave}(m_{12}) + A^l_{S-wave}(m_{13})$. Since this model relies on the assumption that the Isobar model well-describes the higher spin resonances, any limitations of the Isobar Model to describe these resonances may result in leakage to the S-wave. In this study, we present only a first attempt to obtain a fit with the QMIPWA which might need improvements in further research projects.

3
The LHCb experiment

In this chapter, a description of the details of the LHCb experiment including the set up of the equipment, instruments and data processing is provided.

3.1
The Large Hadron Collider (LHC)

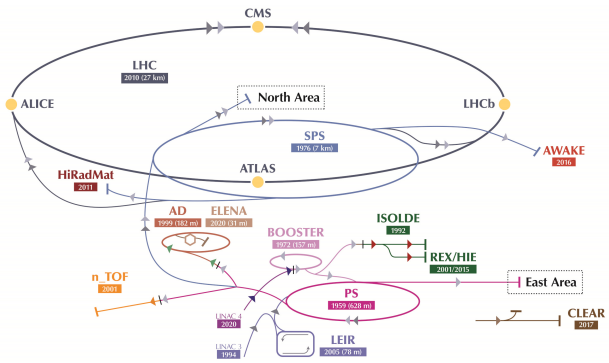

Figure 3.1: Schematic of the CERN accelerators and the Large Hadron Collider

The Large Hadron Collider is the largest synchrotron accelerator and collider in the world located at the CERN laboratory (shown schematically in Fig. 3.1), it consists of a 27-kilometer ring of superconducting magnets with accelerating systems along the path. Two beams of high-energy protons travelling at speeds close to the speed of light are collided inside the accelerator at four main locations corresponding to the positions of the four main detectors: ATLAS, ALICE, CMS and LHCb. The main goal of the experiments performed at the LHC is to find Physics Beyond the Standard Model (BSM) by colliding proton beams at an energy of 13 TeV and luminosity of $L = 10^{32} cm^{-2} s^{-1}$ [1], which is reduced at the LHCb interaction point. Luminosity defined as $N_{event} = L\sigma_{event}$ where N_{event} is the number of events per second generated in the collisions and σ_{event} is the cross section of the event that is being studied. The two high-energy beams of protons travel in opposite directions before they collide.

3.2 The LHCb experiment

The LHCb experiment is one of the main experiments at CERN. It is designed to study heavy flavour physics, interactions involving the heavy quarks c and b [19]. The main goal of the experiment is to search for evidence of new physics through the study of heavy hadron decays including CP violation and mixing [20].

3.2.1 The LHCb detector

The LHCb detector is a single-arm spectrometer with forward angular coverage from approximately 10 mrad to 300 mrad in the bending plane and to 250 mrad in the non-bending plane. This geometry is chosen given that high energy b- and c- hadrons are produced in the same forward or backward cone. A schematic of the detector is shown in Fig. 3.2, where we can appreciate the different components of the detector: a tracking system, a dipole magnet, a particle identification system, calorimeters and muon chambers.

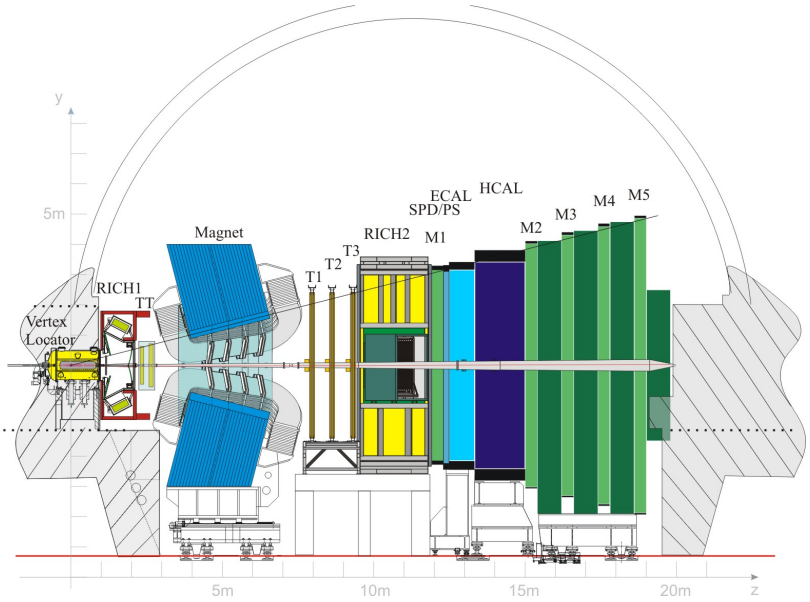

Figure 3.2: Side-view of the LHCb detector. The tracking stations T1-T3 are shown as well as the calorimeters ECAL, HCAL, the magnet, muon chambers M1-M5 and the RICH stations [22].

3.2.2 Tracking system

The tracking system consists of the vertex locator system (VELO) and four planar tracking stations: the Tracker Turicensis (TT) which is located

upstream of the dipole magnet and T1-T3 located downstream of the magnet. VELO is designed to provide precise measurements of the track coordinates close to the interaction region [20] which are used to identify and reconstruct primary and secondary vertices of charm-hadrons, measure the lifetime of these hadrons and the provide measurements of the impact parameter of tag particles. It detects particles with a pseudorapidity in the range $1.6 < \eta < 4.9$ which emerge from primary vertices such that $|z| < 10.6cm$. The VELO is constructed using a series of silicon modules, each one provides values r and ϕ for the position. The data obtained at VELO is used by the TELL1 data processing boards which utilize a set of algorithms that process the raw data to identify clusters which are later used in the trigger and the offline analysis. The Tracker Turicensis is a tracking station with dimensions 150 cm x 130 cm which is located upstream of the dipole magnet and uses silicon microstrip sensors [21].On the other hand, the three T1-T3 stations are made of two components: the Inner Tracker (IT) and the Outer tracker (OT). The ITs are located in the center of the tracking stations and they also use silicon microstrip sensors. Both of the TT and the IT's have four detection layers, each layer consists of seven silicon sensors accommodated into three readout sectors. The Outer Tracker (OT) consist of two layers of straw-tube drift chambers, each tube has an diameter of 4.9 mm filled with a gas mixture of Ar (70%), CO_2 (28.5%) and O_2 (1.5%) with a resolution of 200µm.

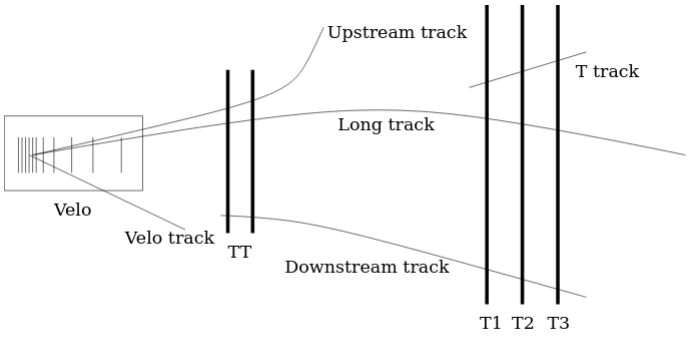

Figure 3.3: Reconstructed track types from the LHCb tracking system. Image taken from [31]

The information obtained by these components is later used to reconstruct tracks. The reconstructed tracks can be classified as (depending on the hits on the different components of the tracking system)[25]:

1. **VELO tracks**, tracks that pass only through the VELO.

2. **Downstream tracks**, tracks that cross the TT and the T1-T3.

3. **Upstream tracks**, tracks crossing only the VELO and TT.

4. **Long tracks**, tracks that have information from all the tracking stations (VELO, TT, T1-T3), therefore they possess the best resolution.

These tracks are schematically shown in Fig. 3.3

3.2.3 Magnet

The dipole magnet bends the trajectories of charged particles and their the momenta are calculated using the radius of the trajectory. The magnetic field generated is inhomogeneous and possesses an integrated bending power of 4 Tm over a 10 m track. The magnet is located downstream of the VELO, RICH1, and TT and it covers the forward acceptance of ±250 mrad vertically and ±300 mrad horizontally. The polarity of this magnet can be inverted in order to reduce systematic errors coming from the asymmetries generated by the detector efficiency.

3.2.4 Particle Identification

Particle Identification of meson decay products is crucial in experiments. The particle identification system is formed by two RICH (Ring-Imaging Cherenkov System) detectors to cover the entire momentum range. The RICH detectors use the Cherenkov radiation produced by the particles that cross dielectric materials inside the detectors. The angle of the Cherenkov radiation cone is related to the momentum of the particle that crosses the dielectric material by the expression: $\cos(\theta_{ch}) = \frac{1}{n\beta}$ where n is the refractive index of the material; together with the reconstructed momentum obtained from the tracking system, we can identify particles by their mass. Cherenkov angles for different particles as function of momentum are shown in Fig. 3.4. The RICH 1 is used to identify low-momentum particles in the range $\sim 1 - 60$ GeV/c using aerogel and it is located upstream of the magnet between the VELO and the Tracker Turicensis in the region $990 < z < 2165$ mm. On the other hand, the RICH 2 is used to cover the high-momentum range from ~ 15 GeV/c up to 100 GeV/c using CF4 radiator and it is located between the last tracking station and the first muon chamber. Both of the RICH detectors have spherical and flat mirrors used for focusing of the Cherenkov light. Additionally, Hybrid Photon Detectors (HPDs) are included in the particle identification system to detect the Cherenkov photons in the wavelength range 200-600 nm.

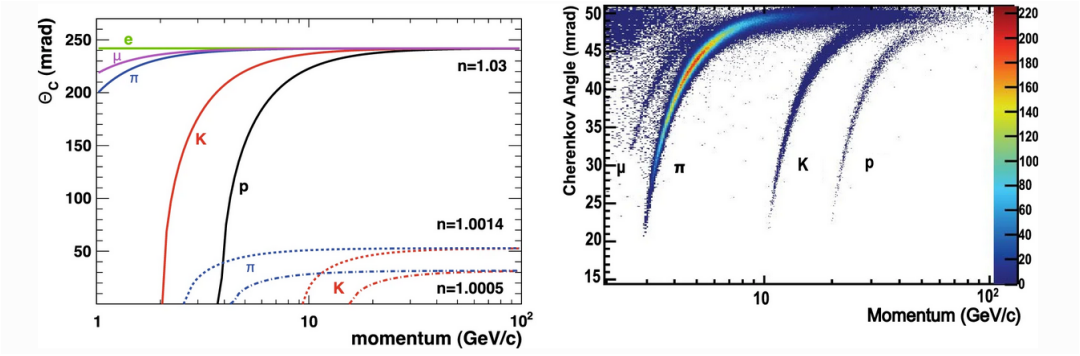

Figure 3.4: Cherenkov angles for the different radiators as a function of momentum (left). The measurement of the RICH performance in the data for two radiators (right). Image taken from [26]

3.2.5 Calorimeters

The calorimeter system selects high tranverse energy hadron, electron and photon candidates for the first trigger level (L0). It helps in the identification of electrons, photons and hadrons and measures their energies and positions. These particles produce new particles with lower energy in cascades which are called "showers" and the calorimeters can determine energy and positions of the particles based on the produced showers. The calorimeter system consists of a pre-shower detector (PS) followed by scintillator pad detector (SPD) which selects charged particles, the main electromagnetic calorimeter (ECAL) and a hadron calorimeter (HCAL). The ECAL is chosen to be 25 radiation lengths thick in order to fully contain showers generated by high energy photons therefore achieving an optimal energy resolution. No such condition applies to the HCAL so its thickness is chosen to be 5.6 radiation lengths due to space limitations. The calorimeters receive scintillating light which is then transmitted to a Photomultiplier by wavelength-shifting fibers. In the case of the SPD and PS, the single fibers are read out using multi-anode photomultiplier tubes and in the case of the ECAL and HCAL, the fibre bunches have individual phototubes.

3.2.6 Muon Chambers

Muons play an important role in the measurements of CP asymmetry and particle oscillations given that muons from semi-leptonic decays provide a tag of the initial state flavour. The muon system provides information to the Level-0 trigger and the High-Level trigger and it is composed by five stations

(M1-M5) placed along the axis, the full system has 1380 chambers within an area of 435 m^2. M2-M5 are all located downstream of the calorimeters and interconnected by iron-absorbers to avoid background hadrons. Station M1 is located before the calorimeters so that the p_T measurement in the trigger is improved. M1-M3 have a high spatial resolution and they are used to determine the direction of the track and to calculate the p_T of a muon candidate with a resolution of 20%. On the other hand, the stations M4-M5 have a limited spatial resolution, therefore their purpose is mainly the identification of penetrating particles. The muon trigger uses the muon reconstructed track and the measurement of the p_T which requires that the hits are alligned in all the 5 stations.

3.2.7 Trigger

The LHC has a bunch-crossing frequency of about 40 MHz, where the crossing frequency with interactions visible by the LHCb is about 10 MHz (visible meaning that at least two charged particles are produced with sufficient hits in the VELO and T1-T3 to allow the reconstruction of the event). This frequency needs to be reduced to a few kHz by the trigger in order to allow the storage of events which are relevant for further offline analysis. The trigger consists of two levels: Level-0 (L0) and the High Level Trigger (HLT). The L0 trigger operates using custom made electronics and its purpose is to reduce the 40 MHz beam crossing rate of the LHC to a lower rate of 1 MHz. This is achieved by the selection of the particles with large tranverse momentum (p_T) and large transverse energy (E_T). The L0-trigger is divided in three sub-components: the pile-up system, the L0-calorimeter and L0-muon trigger; each of these components is connected to a detector and to the L0 Decision Unit (DU) which makes the final decision based on the information obtained from the trigger systems. The pile-up system calculates the position of the primary vertices along the beam-line which are used to distinguish crossings with single and multiple interactions. The Calorimeter trigger selects high E_T electrons, photons or hadrons, then these clusters are identified as the different particles based on the information provided by SPD, PS, ECAL and HCAL. Also, the number of hits in the SPD are used to estimate the number of tracks. The muon trigger uses the data from the five muons stations to form tracks and it selects the two muons with the highest p_T for each quadrant of the muon detector. Then, a DU uses all the information obtained for these quantities and delivers a final L0-trigger decision for each bunch crossing. The time between a pp interaction and the arrival of the decision is set to 4 μs. The High Level

Trigger (HLT) is performed with a C++ application which runs on every CPU of the Event Filter Farm (EFF). The HLT is sub-divided in two stages: the HLT1 and the HLT2. The purpose of the HLT1 is to reconstruct particles in the VELO and the T-stations in order to reduce the rate to 30 kHz. This is called L0 confirmation and it is done to allow full event reconstruction in the HLT2. The HLT2 combines inclusive (partial reconstruction) and exclusive (full reconstruction) algorithms to perform the selection of the final states.

4
Data selection

The data selection of the LHCb Run 2 data obtained for the $D_s^+ \to K^-K^+K^+$ decay channel was mostly performed by Carolina Bolognani in [27] (this study was dedicated to the search of CP violation in the decay channels: $D^+ \to K^-K^+K^+$ and $D_s^+ \to K^-K^+K^+$). These selection requirements were intended to reduce the background distribution of the data sample and for this reason they were also needed in this study. Therefore, the data sample after almost all selection requirements described in [27] was used in this work. Later, futher analysis criteria was imposed to obtain a suitable sample for the amplitude analysis presented in this dissertation. Final elements needed for the fitting procedure were constructed and their description is given in Chapter 5. A summarized description of the steps of the data selection is provided here for completeness.

4.1
Variables

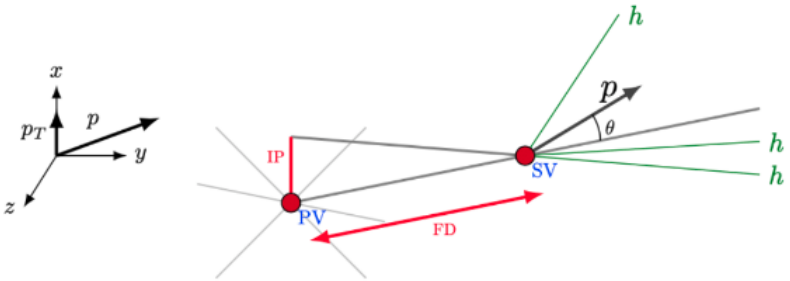

Figure 4.1: Topological variables involved in the particle decay.

The analysis of the decay $D_s^+ \to K^+K^+K^-$ is performed using the information provided by the detector, trigger and reconstruction software. From the detector, a set of topological variables are obtained for each detected event. A list of the variables used in the analysis is shown below:

– **Mass** $(K^+K^+K^-)$ → The combined invariant mass of the three kaon candidates.

- $\mathbf{s}_{12/13}$ → Invariant mass squared for the particle systems $P1$-$P2$ and $P1$-$P3$.
- **Primary Vertex** (**PV**) → Position of the D_s^+ candidate production.
- **Secondary Vertex** (**SV**) → Position of the D_s^+ candidate decay.
- **Flight distance** (**FD**) → Distance between the primary and secondary vertices.
- **Impact parameter** (**IP**) → Minimum distance between the primary vertex and the particle's trajectory.
- **Momentum** (p) → Magnitude of the particle's reconstructed momentum.
- **Transverse momentum** (p_T) → Component of the momentum perpendicular to the beam axis
- **Lifetime** → Decay time of the D_s candidate.
- **Direction angle (DIRA)** → Cosine of the angle between the particle's momentum and the direction of the vector from PV to SV.
- **Vertex** χ^2 → Quantitative measurement of the quality of the reconstructed secondary vertex from the three particle tracks.
- **IP** χ^2 → Quantitative measurement of the quality of the impact parameter.
- **Track** χ^2 → Quantitative measurement of the quality of the reconstructed track.
- **Pseudorapidity** (η) → Measurement of the angle of the particle track relative to the beam axis, $\eta = -\ln[\tan\frac{\theta}{2}]$
- **PIDK** → Information on particle identification obtained from the RICH, defined as the delta-log-likelihood of a particle being a kaon with respect to the pion hypothesis PIDK$= \Delta\log\mathcal{L} = \frac{\mathcal{L}_K}{\mathcal{L}_\pi}$.
- **ProbNNk** → Probability value of a particle being a kaon obtained from multi-variate analysis obtained from combining tracking and PID information.

Experimentally the reconstructed mass of the D_s^+ candidates follows a distribution coming from the momentum resolution of the reconstructed particle tracks. For this reason, the Dalitz plot extends beyond the theoretical borders defined in Eq. 2-19. In order to account for this problem, a package known as DecayTree Fitter (DTF) is used; it changes the momentum of the particles within their corresponding uncertainties so that the D_s^+ candidates' mass values are forced into the D_s nominal mass, this ensures that the events fall

Daughter requirements	
χ^2_{Track}/ dof	< 3.0
p_T [MeV]	>250
χ^2_{IP} wrt any PV	> 4
PIDK $= \Delta \log \mathcal{L}_{K\pi}$	> 5
Combination requirements	
Mass [MeV]	1879 - 2059
$\sum p_T$ [MeV]	> 3000
p_T at least one track [MeV]	> 1000
p_T at least two tracks [MeV]	> 400
IP χ^2	> 10 (at least one track)
IP χ^2	> 4 (at least two tracks)
Mother requirements	
Mass [MeV]	1879 - 2059
Track vertex χ^2/dof	<10
Lifetime [ps]	> 0.2
acos(DIRA) [mrad]	> 14.1

Table 4.1: HLT2 selection criteria

within their physical phase space, inside the theoretical Dalitz plot. In this amplitude analysis, we construct the Dalitz plot using DTF invariant masses squared.

4.2 Data samples

This analyis is performed using the data collected by the LHCb detector during the time period 2016-2018 from proton-proton collisions at center of mass energy $\sqrt{s} = 13$ TeV (which is known as Run 2). This data corresponds to an integrated luminosity of 5.6 fb^{-1} and comes from the HLT2 trigger. The HLT2 performs an online full reconstruction of events and data selection requirements which are based on decay variables. These requirements shown in Table 4.1. These requirements are chosen so that the D_s candidates' mass and the reconstructed mass lies within a range including the nominal mass of the D_s meson; also a good vertex resolution is required, the momentum should be consistent with the mass of the particles, the lifetime of the D_s is required to be large and a good kaon identification is necessary.

4.3 Offline selection

After the trigger selection, offline selection requirements are needed due to the still high background level in the samples. The first step in the analysis

is to define further selection requirements to deal with the remaining sources of background; this is done by using the data sample collected in 2016. The first pre-selection is shown in Table 4.2. These are a set of kinematic requirements including cuts on the mass spectrum and IP χ^2 of the D_s candidate. To further continue the analysis and to reduce the background from the sample, the invariant mass distribution M of the D_s is used, the invariant mass distribution is shown in Fig. 4.2. As it can be seen in Fig. 4.2, the data sample has significant contribution from different background sources. The kinematic variables given in the data sample are used to reduce combinatorial background (background coming from the association of three random tracks) and specific background which comes from cross-feed with other channels, clone tracks and high charge asymmetry regions arising from parts of the detector.

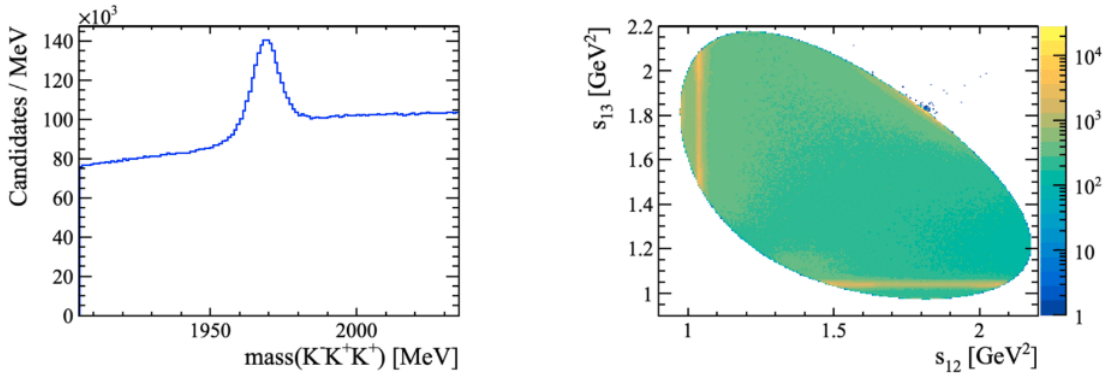

Figure 4.2: D_s^+ reconstructed mass distribution from the 2016 LHCb data sample (left). The Dalitz plot obtained from this data set is shown on the right. Image taken from [27]

In order to decide the selection criteria to deal with the combinatorial background, the quantity known as the signal significance is introduced and defined as:

$$Significance = \frac{S}{\sqrt{S+B}} \tag{4-1}$$

where S and B are the number of signal and background events respectively inside the signal region of the mass distribution. In order to obtain S, the background events are subtracted from the signal region using the background region distribution (region outside the mass distribution peak) and assuming a linear distribution of these events over the entire spectrum. The signal region is defined as R_{signal} = 1960<M<1980 [MeV] and the background region is defined as $R_{background}$ = (1920<M<1930) ∪ (2010<M<2020) [MeV].

nSPDHits $<$ 1000
$1.5 < \eta_{daughters} < 5$
$p_{daughters} < 100$ GeV
IP χ^2 <15
1905<M<2035 MeV

Table 4.2: Additional pre-selection requirements [27]

4.3.1 Specific Background sources: Charm background

A contribution to the specific background is the mis-identification of a given daughter particle causing a cross-feed from other decay channels. By looking at the mass distribution of the data sample shown in Fig. 4.2, we can clearly see a contamination at the right sideband (the bump right next to the signal peak) associated to the decay channel $D^+ \to K^-K^+\pi^+$ resulting from the mis-ID of a pion as a kaon. This contribution can be reduced by imposing requirements on the PID variables: PIDK and ProbNNk. Both PIDK and ProbNNk variables are tested in order to reduce the D^+ peak in a mass spectrum where the mass of the candidate is reconstructed by assigning the pion mass to one of the daughters instead of the kaon mass. Since the mis-identification can occur with either of the two K^+, the same variable cuts are applied on both of them. The $KK\pi$ invariant mass distributions are shown for different values of PIDK requirement in Fig. 4.3, as it can be appreciated the $D^+ \to K^-K^+\pi^+$ contribution is significantly reduced for PIDK$_{2,3}$>15. No PID requirement is applied for the K^- because there does not exist specific backgrounds due to mis-ID of this kaon.

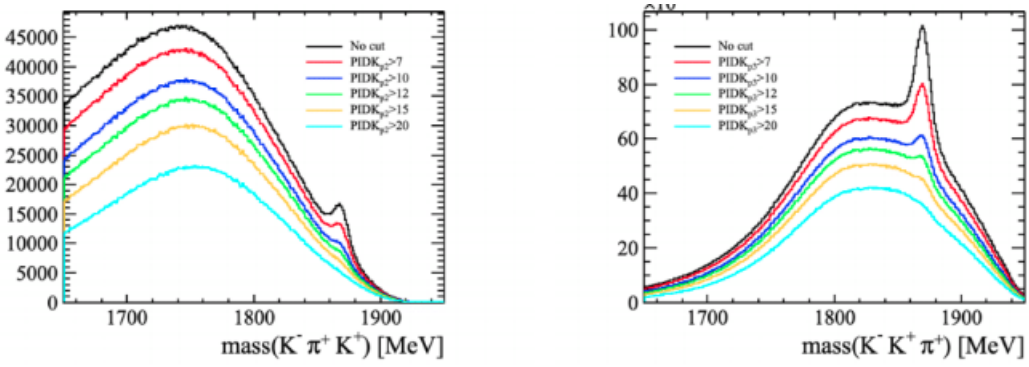

Figure 4.3: Invariant mass reconstructed by assigning the π to the K^+ daughter of lowest (left) and highest (right) momentum. The invariant mass is shown for different values of PIDK requirements in different colors. Image taken from [27]

4.3.2
Specific background sources: Clones and charge asymmetries

Sometimes in the process of reconstruction, a single track can be wrongly duplicated and a pair of kaons in the data sample might come from a single track. This background contribution can be seen in the Dalitz plot of Fig. 4.2 as a concentration of events in the region next to the border that is closest to the top-right corner (the high concentration of blue points in the right hand side image of Fig. 4.2), region in which $p_2 = p_3$ and corresponding to the lowest K^+ momenta. In order to suppress the contributions coming from clone tracks in the data sample, two variables: difTX23 and difY23 are defined. The mathematical expressions for these variables are shown in Eq. 4-2.

$$\text{difTX23} = \left|\frac{p_{x_2}}{p_{z_2}} - \frac{p_{x_3}}{p_{z_3}}\right| \quad , \quad \text{difTY23} = \left|\frac{p_{y_2}}{p_{z_2}} - \frac{p_{y_3}}{p_{z_3}}\right| \tag{4-2}$$

.

We can clearly see a peak in the distributions of these variables, shown in Fig. 4.4 which comes from a contribution of the clones near zero. The cuts applied to these variables were performed in such a way that the efficiency is over 99% and a good significance is mantained. The applied requirements on these variables are difTX23 $> 2.3 \times 10^{-3}$, difTY23 $> 2.3 \times 10^{-3}$.

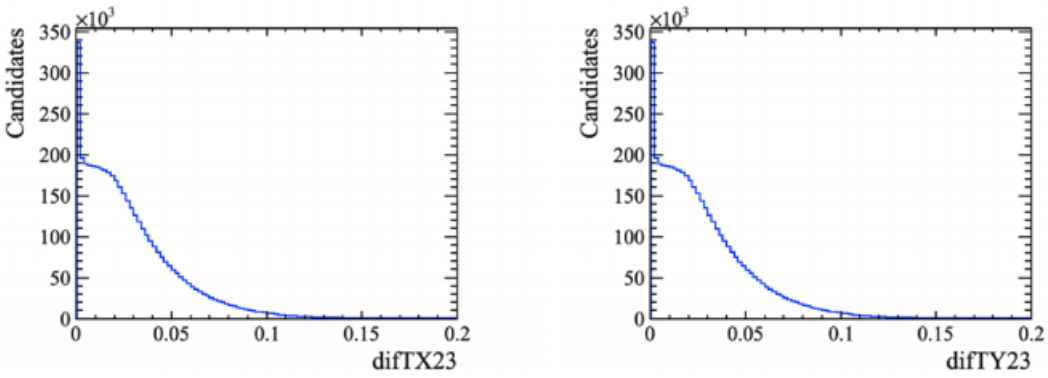

Figure 4.4: difTX23 (left) and difTY23 (right) variable distributions. Image taken from [27]

On the other hand, charge asymmetries are generated when low momentum tracks are driven away from the detector. To reduce these contributions, requirements are chosen in such a way that the high asymmetry regions are

removed from the data sample, these requirements are

$$\begin{aligned} p_{z_{1,2,3}} &> 1 + 3.57 \times \left|p_{x_{1,2,3}}\right| \text{[GeV]} \\ p_{z_{1,2,3}} &> 4.25 \times \left|p_{y_{1,2,3}}\right| \text{[GeV]} \\ p_{z_{1,2}} &> 4\text{[GeV]}. \end{aligned} \tag{4-3}$$

These cuts have a relative efficiency of 96%.

4.3.3 Multi-variate analysis

The last step in the offline selection is the application of a multi-variate analysis to select the signal candidates given that the remaining background cannot be reduced by other specific requirements. This tool is designed in such a way that a classifier is trained to distinguish between signal and background distributions using several discriminatory variables of a test data sample; then a value is assigned to the decision classifier variable for each event. This response is later applied to a larger data sample where a decision variable is obtained for each event and finally a requirement on this variable is imposed to reduce the background contribution.

This technique is based on a Boosted Decision Tree (BDT) classifier which uses a binary tree that makes decisions on one variable at a time. A 50k-event data sub-sample from the 2016 data set is used in the training and testing phase. In order to perform the training, pure signal and background samples should be given to the classifier for the analysis. These background and signal distributions are obtained through the use of the sPlot method implemented in the ROOT package. The sPlot technique is based on a fit of the data sample using provided probability distribution functions (PDFs) for the signal and background components of the invariant mass spectrum. Then, the sPlot algorithm provides a weight for each event, weight that is associated to the probability of that event being signal or background (based on the fit performed using the RooFit package [23]).

In this case, the signal PDF is modelled as the sum of a Gaussian and two Crystal Ball PDF's (the two Crystal Balls are provided to account for the tails on both sides of the signal peak) as shown in the equation below:

$$\begin{aligned} \mathcal{P}_{sig}(m) = f_G \times G(\mu, \sigma_G) + (1 - f_G) \times [f_{\text{CB}} \times \text{CB}_1(\mu, R_1\sigma_G, \alpha_1, N_1) \\ +(1 - f_{\text{CB}}) \times \text{CB}_2(\mu, R_2\sigma_G, \alpha_2, N_2)] \end{aligned} \tag{4-4}$$

where R_1 and R_2 are included so that the σ's of the Crystal Balls are related

to the σ_G of the Gaussian PDF; the f_G and f_{CB} are fractions related to the Gaussian and one of the Crystall balls and they are included so that the total PDF is normalized. The Crystal Ball distribution is given by the equation:

$$\mathrm{CB}(m|\mu,\sigma,\alpha,N) = \mathcal{N}\begin{cases}\exp\left(-\frac{(m-\mu)^2}{2\sigma^2}\right), & \text{for}\,\frac{m-\mu}{\sigma} > -\alpha \\ A\cdot\left(B-\frac{m-\mu}{\sigma}\right)^{-N}, & \text{for}\,\frac{m-\mu}{\sigma} \leq -\alpha\end{cases} \tag{4-5}$$

where $A = \left(\frac{N}{|\alpha|}\right)^N \exp\left(-\frac{|\alpha|^2}{2}\right)$, $B = \frac{N}{|\alpha|} - |\alpha|$, $\mathcal{N} = \frac{1}{\sigma(C+D)}$, $C = \frac{N}{|\alpha|}\frac{1}{N-1}\exp\left(-\frac{|\alpha|^2}{2}\right)$ and $D = \sqrt{\frac{\pi}{2}}\left(1+\mathrm{erf}\left(\frac{|\alpha|}{\sqrt{2}}\right)\right)$. On the other hand, the background's PDF is chosen to be a third-order Bernstein polynomial. The expression for the background PDF is shown in Eq. 4-6.

$$\mathcal{P}_{bkg}(m) = \sum_{i=0}^{3} a_i \binom{n}{i} m^i (1-m)^{n-i} \tag{4-6}$$

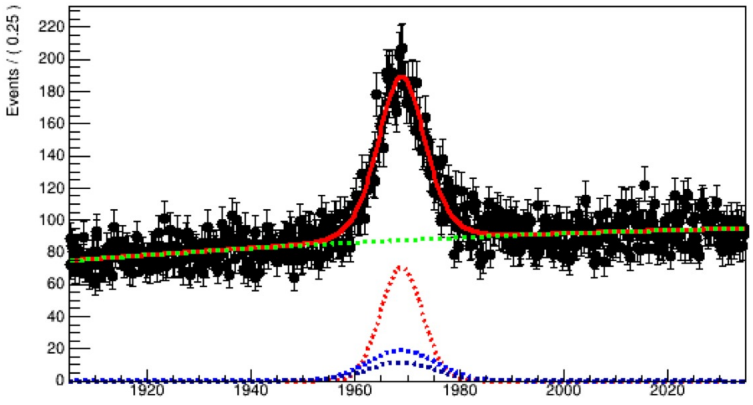

Figure 4.5: Invariant mass fit for a 50k event sub-sample after all selection requirements. Image taken from [27].

From the 50k-event training sub-sample, half of the events is used for actual training and the other half for testing. The invariant mass fit for this subsample is shown in Fig. 4.5. Ten variables are used for the training and testing, variables corresponding to the parent particle and symmetric contributions from the daughters: IP, IP^2_χ, Combination log IP, FD, $\log(\mathrm{FD}^2_\chi)$, DIRA, p_T and p. The results are then applied in the remaining samples (data sets collected in the time period 2016-2018) after applying all the offline selection requirements and excluding the 50k-event used for the training. Finally, a BDT value is assigned to every event in the sample. In the analysis performed by Carolina Bolognani in [27], the BDT requirement was set to

BDT>-0.02 obtaining a purity[1] of 64.44±0.04% which was suitable for the search of CP violation performed in [27].

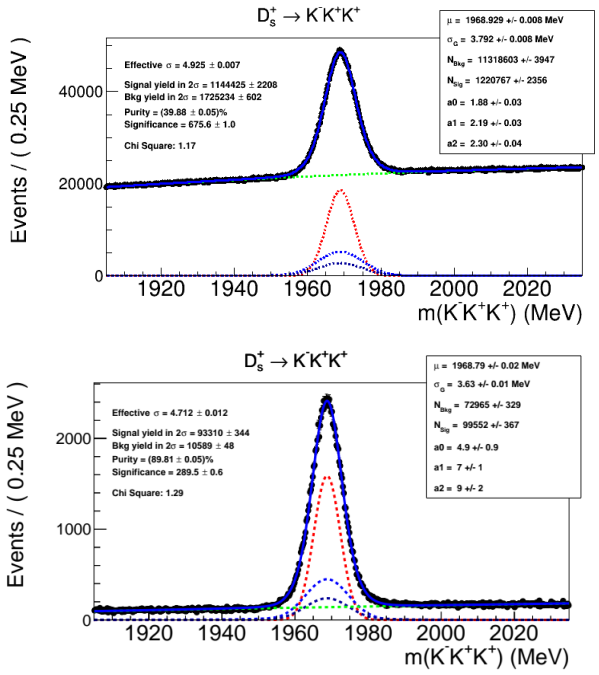

Figure 4.6: Mass fit of the data sample including all data sets in Run 2 (2016-2018) and after all pre-selection and selection requirements. The top figure shows the distribution before BDT cut and the bottom figure shows the distribution after BDT>0.16 cut.

On the other hand, an amplitude analysis requires a sample with higher purity to avoid large systematic uncertainty due to the background parametrization. In order to achieve a higher purity in the sample, the requirement on the BDT value had to be adjusted so that a purity of approximately 90% in the final sample is obtained. The BDT requirement was set to BDT>0.16 yielding a purity of $89.81 \pm 0.05\%$ as it can be seen in Fig. 4.6. Table 4.3 summarizes all the offline selection performed in the data sample.

Using the standard deviation obtained in the fit, σ_G (the standard deviation of the Gaussian PDF), we can introduce σ_{eff} (defined in Eq. 4-7) which is used to obtain the signal region; region that is within $2\sigma_{eff}$ of the mean μ also obtained in the fit. In the case of the fit shown in Fig. 4.6, the

[1]Purity is defined as $\frac{N_s}{N_s+N_b}$ where N_s and N_b are the number of signal and background events respectively in the signal region. Additionally to this, the signal region is related to the invariant mass fit shown in Fig. 4.6 such that $\mu - 2\sigma_{eff} \leq M \leq \mu + 2\sigma_{eff}$, $1968.8 \leq M \leq 1978.2$ [MeV].

Pre-selection	nSPDHits < 1000 $1.5 < \eta_{products} < 5$ $p_{daughters} < 100$ GeV $\mathrm{IP}_{\chi^2} < 15$ $1905 < \mathrm{M} < 2035$ MeV
ID requirements	$\mathrm{PIDK}_{2,3} > 15$
Clone requirements	difTX23$>2.3\times10^{-3}$
Fiducial requirements	$p_{z_{1,2,3}} > 1 + 3.57 \times\lvert p_{x_{1,2,3}}\rvert$ GeV $p_{z_{1,2,3}} > 4.25 \times\lvert p_{y_{1,2,3}}\rvert$ GeV $p_{z_{1,2}} > 4$ GeV
BDT requirement	BDT>0.16

Table 4.3: Summary of pre-selection and selection requirements performed in the entire data set (2016, 2017, 2018 samples) for the decay $D_s \rightarrow K^-K^+K^+$[27].

signal region is (1959.37-1978.21) [MeV] with a $\sigma_{eff} = 4.712\pm0.012$ MeV where the number of signal events inside the signal region is $N_{sig} = 93310 \pm 344$.

$$\sigma_{eff} = \sqrt{f_G\sigma_G^2 + (1-f_G)\times(R_1\sigma_G)^2 + (1-f_G)\times(1-f_1)\times(R_2\sigma_G)^2} \quad (4\text{-}7)$$

After performing all selection requirements, the Dalitz plot of the phase space for the decay channel $D_s^+ \rightarrow K^-K^+K^+$ constructed using the selected data sample is shown in Fig. 4.7. We can appreciate a clear contribution from the $\phi(1020)$ resonance presented as a thin line close to the region $s_{K^-K^+} \approx 1.2$ GeV^2 together with its characteristic angular distribution. Also, a S-wave structure is present close to the theoretical lower border of the Dalitz plot. This S-wave interfers with the $\phi(1020)$ resonance distording the bands of the $\phi(1020)$. Also, the DP is slightly populated at high invariant mass squared which imposes a challenge in the fitting procedure.

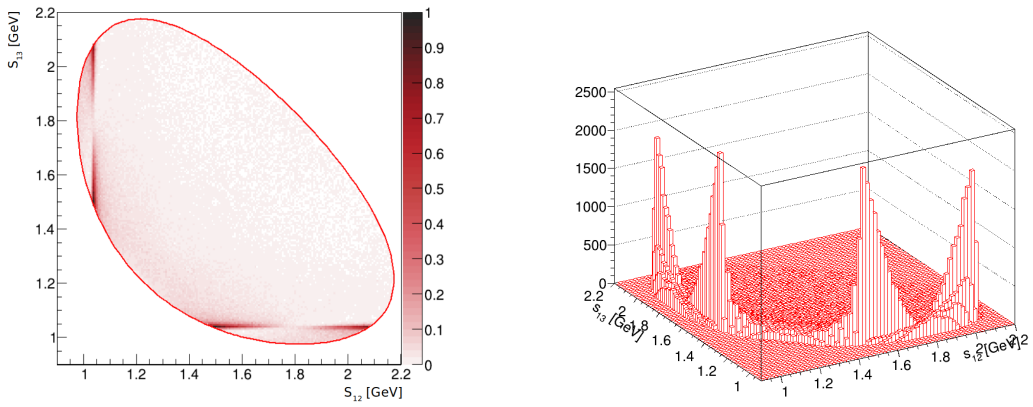

Figure 4.7: Dalitz Plot of the data sample corresponding to the decay $D_s^+ \to K^-K^+K^+$. Two drawing options are used to better appreciate the resonant structure.

5
Fitting procedure, Efficiency map and Background studies

The goal of an amplitude analysis is to describe the dynamics (resonant structure) of a decay using phenomenological models. In the ampliude analysis described in this dissertation, the models used are the Isobar Model and the Quasi-Model Independent Partial Wave Analysis (QMIPWA). The fitting procedure in the analysis presented in this work was performed using the GooFit package which is an interface that uses a minimisation algorithm called MINUIT and Graphics Processing Unit (GPU) to evaluate the probability density functions provided [14]. Aside from the selection performed to the data set, it was also necessary to obtain a parametrization of the background distribution in the signal region (the signal region contains approximately 10% of background events) and to account for the effects of the detector in the structure of the Dalitz plot (efficiency). The effects of the detector are accounted by the construction of an efficiency map represented by a 2D histogram. On the other hand, the background is also parametrized by a 2D histogram and it is obtained after performing background studies described in this section. In this chapter, a brief description of the fitting procedure used for this amplitude analysis is provided and the efficiency and background parametrizations are also described.

5.1
Fitting procedure

The data fit is performed using the maximum likelihood estimation (MLE), a method of statistical inference, which is based on testing hypothesis or deriving estimates to infer properties of a data set. Let a data set with points represented by the vector: $\boldsymbol{x} : x_1, ..., x_N$ and let a probability density function (PDF): $f(x;\theta)$ which depends on a set of parameters $\boldsymbol{\theta} : \theta_1, ...\theta_n)$. This PDF supposedly describes the distribution of these points. Using this PDF, we can define a function known as likelihood function, which expression is given in Eq. 5-1.

$$\mathcal{L}(\boldsymbol{x};\boldsymbol{\theta}) = \prod_{i=1}^{N} f(x_i;\boldsymbol{\theta}) \tag{5-1}$$

This likelihood function can be also used to define a quantity called FCN which is given by the following expression:

$$\text{FCN} = -2\log\mathcal{L} = -2\sum_{i=1}^{N} f(x_i;\boldsymbol{\theta}); \tag{5-2}$$

the models with lowest FCN are considered as the models that better describe our data set. The goal of the MLE is to obtain the set of parameters that maximizes the likelihood function $\mathcal{L}$ which is equivalent to minimizing the FCN. Minimizing the FCN is easier than maximizing the likelihood since each term in the FCN is independent of the others. In the fitting procedure, not only the phenomenological models given to describe the amplitude are contemplated but also the detection efficiency and the background distribution across the Dalitz plot. Therefore, the total PDF of our model, f, is given by the normalized sum of signal and background components:

$$f(s_{12}, s_{13};\boldsymbol{\theta}) = f_{sig}\mathcal{P}_{sig}(s_{12}, s_{13};\boldsymbol{\theta}) + (1 - f_{sig})\mathcal{P}_{bkg}(s_{12}, s_{13}), \tag{5-3}$$

the fraction f_{sig} is the relative fraction of the signal events remaining in the data sample after selection (in our case $f_{sig} \cong 0.9$ as mentioned in the previous chapter). $\mathcal{P}_{bkg}$ is obtained as a 2D histogram background studies, described below. $\mathcal{P}_{sig}$ is explicitly given by the equation below:

$$\mathcal{P}_{sig} = \frac{|\mathcal{M}_{s_{12},s_{13}}|^2\epsilon(s_{12}, s_{13})}{\iint_{DP}|\mathcal{M}_{s_{12},s_{13}}|^2\epsilon(s_{12}, s_{13})ds_{12}ds_{13}}. \tag{5-4}$$

where $\mathcal{M}$ is the amplitude of the decay (given by the phenomelogical models: Isobar and QMIPWA, described in Chapter 2), additionally a normalization is included in the PDF and $\epsilon(s_{12}, s_{13})$ is the efficiency map which provides a correction for the detection efficiency. The set of parameters to be found are the magnitudes a_i and phases δ_i of the complex coefficients in the Isobar model. In the case of the QMIPWA, we also look for the amplitude and phase of the S-wave in the bins provided.

5.1.1 Fit Fractions

The fit fractions are quantities often used in amplitude analyses and they can provide a qualitative description for the components of the phase space of a decay. These fit fractions are independent of the convention used in different fitting programs like the amplitude formalism, normalization and phase convention. These fit fractions are useful when comparing the results

obtained in different analyses. The mathematical expression for the fit fractions is shown in Eq. 5-5.

$$FF_i = \frac{\int\int_{DP} |c_i \mathcal{A}_i(s_{12}, s_{13})|^2 ds_{12} ds_{13}}{\int\int_{DP} |\sum_j c_j \mathcal{A}_j(s_{12}, s_{13})|^2 ds_{12} ds_{13}} \tag{5-5}$$

The fit fractions do not necessarily add to one as it can be appreciated in Eq. 5-5 due to the interference among the different resonances. In this context, we can also define the interference fit fractions (given in Eq. 5-6) that together with the fit fractions add up to one:

$$FF_{ij} = \frac{\int\int_{DP} 2\mathrm{Re}|c_i c_j^* \mathcal{A}_i(s_{12}, s_{13}) \mathcal{A}_j^*(s_{12}, s_{13})| ds_{12} ds_{13}}{\int\int_{DP} |\sum_j c_j \mathcal{A}_j(s_{12}, s_{13})|^2 ds_{12} ds_{13}} \tag{5-6}$$

In Eq. 5-6, the interference fit fractions are only defined for a pair of resonance amplitudes $\mathcal{A}_i$ and $\mathcal{A}_j$ such that $\mathcal{A}_i \neq \mathcal{A}_j$ and the integration is performed over the entire phase space of the decay.

5.2 Efficiency map

In order to account for the effects of the detection efficiency, it is necessary to obtain a parametrization for the detection efficiency across the Dalitz plot as a function of the invariant masses squared, s_{12} and s_{13}. This efficiency map is constructed as a 2D histogram from a simulation (Monte Carlo) sample generated using the LHCb software as a function of the Dalitz plot coordinates.

The simulation sample is generated using the framework Gauss [38], the events are generated using Pythia 8 [37] which simulates actual proton-proton collisions accounting for generation and detection. Heavy hadrons produced in these collisions are generated using `EvtGen` [39]. Later, the propagation of particles and interaction with the detector are simulated using GEANT4 [40]. Since it did not exist a theoretical model for the phase of the decay $D_s^+ \to K^-K^+K^+$ (when the simulation was run), the MC sample was generated without a resonant structure (constant matrix element) so it only contains information about the kinematical boundaries of the decay and the detection efficiency.

The first step in the efficiency map construction is the application of the same selection criteria to the MC as the requirements applied to the data sample, the same reconstruction, (L0, HLT1, HLT2) trigger, stripping and MVA selection. Additional to these requirements, the MC is corrected to account for differences in the distributions of the kinematical variables with respect to data. This process is performed by a reweighting algorithm.

5.2.1 Resonant structure weight

Before the reweighting procedure, it is necessary to include the resonant behavior of the decay in the simulation sample. As mentioned before, the simulation is generated using a constant matrix element so that the resonant structure of the $D_s^+ \to K^-K^+K^+$ decay is not present in the distributions of the variables in the MC. This resonant structure can be incorporated into the MC by the use of a resonant structure weight. This weight is constructed from a 2D histogram of the data sample after correcting for the detection efficiency and subtracting the background contributions.

This is achieved in the following way: First, the invariant mass distribution of the data sample (after performing all the selection requirements) is fitted using the Splot technique [15] with the same PDF described in Chapter 4 (signal: Gaussian and two crystal balls, Eq. 4-4 and background: Bernstein polynomial, Eq. 4-6). Then, a Dalitz plot is constructed using the invariant masses squared s_{12} and s_{13} weighted by the results obtained in the Splot which should subtract the background contribution (these weights are related to the probability of an event being signal or background). Then, a Dalitz plot of the MC is constructed weighted by the PID correction (this DP is supposed to account for the efficiency). Finally, the ratio between these two histograms is taken. Given that the sPlot accounts for the background distribution and the MC accounts for the efficiency, the final histogram should only contain the resonant structure of the decay. The final histogram is used to obtain the resonant structure weight (the weight of an event is given by the height at the position of that event in the final histogram). The histogram of the resonant structure is shown in Fig. B.1 in Appendix B.

5.2.2 Reweighting

The next step in the construction of the efficiency map is the kinematical reweighting of the MC events. This process ensures that any remaining difference between the distributions of the MC and the data sample for relevant variables are accounted for. The reweighting algorithm consists in calculating weights using estimators in the same way that the MVA algorithm is implemented, details on how the algorithm works can be found in [41]. However, the reweighting does not return a value for a decision classifier but a weight for each event. The reweighting algorithm works with two samples that are provided to the classifier. The first sample is called the original sample (in our case the MC) and it is the one that requires the corrections; the second

sample is called the target which in this case is the data sample. The variables provided to the reweighting classifier in our case are related to the mother particle: p, p_T, ETA, FD χ^2, IP χ^2, DIRA, FD, IP and Vertex χ^2. Additionally to this, the data sample includes the signal weights obtained from the sPlot technique (which accounts for the background distribution in the sample) and the MC includes the PID and resonant structure corrections in the reweighting. To obtain the reweigthing correction, we use an algorithm known as folding reweighter which divides the sample on a given number of sub-samples and each one is used for the training. Then, the results obtained are applied to the remaining samples. In the our reweighting process, 3 folds were used. The distributions of the variables before and after the reweighting are shown in Appendix B where it can be clearly seen how this process equalized the distributions.

5.2.3 Efficiency map construction

As mentioned above, the efficiency map in the fitting procedure is provided as a 2D histogram. The height of a bin in a given position (s_{12}, s_{13}) will provide a value for the efficiency at that point. The efficiency is constructed by filling a 2D histogram with MC events weighted by the PID and the reweighting corrections. In addition to this, the border of the Dalitz plot should also have corrections since it may be less populated than the rest of the phase space due to binning effects. To account for this, we divided the MC histogram by a histogram constructed using a larger sample of events (about 40 million) generated in GooFit with a constant matrix element. Finally, we use a 2D cubic spline to produce a smoothed histogram to account for the statistical fluctuations. The cubic spline is performed using the LauCubicSpline code from Laura++ [7]. The final efficiency histogram is shown in Fig. 5.1.

5.3 Background parametrization

Similarly to the efficiency, the background is parametrized as a 2D histogram. In principle, the background histogram could be constructed by simply plotting a Dalitz plot populated with the events in the background region of the mass spectrum ($\{1925<M<1955\}\cup\{1985<M<2025\}$), this is possible since the background distribution is linear across the whole spectrum. However, the $\phi(1020)$ present in the background would be distorded due to the use of DFT invariant masses squared. The DTF makes the $\phi(1020)$ peak move slightly from the expected position so the $\phi(1020)$ will be wider than expected

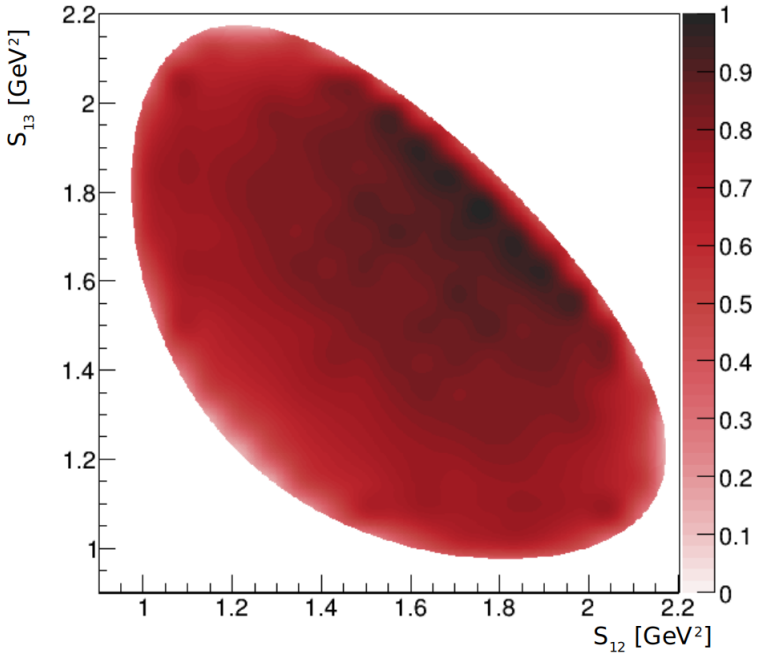

Figure 5.1: Corrected efficiency map used in the $D_s^+ \to K^-K^+K^+$ fits.

in the background DP. This is ilustrated in Fig. 5.2 where the invariant mass squared distributions for two different slices of the background region are shown. It is clear that the $\phi(1020)$ peak is shifted from the expected position. For this reason, another method has to be used to construct the background histogram. The method used in this dissertation is known as background studies.

Since the background contribution is linear across the invariant mass spectrum, a parametrization for this distribution can be obtained in different slices of the background region and then these results can be used to "interpolate" a parametrization for the background inside the signal region $(1968.8 \leq M \leq 1978.2)$ [MeV].

In order to obtain the background parametrization for different slices of the background region, we performed 1D fits of the $s_{K^-K^+}$ distributions in those slices. The PDFs used for these fits contains three main components: $\phi(1020)$, $f_0(980)$ and the non-resonant phase space as shown in the equation below:

$$B(s) = N_\phi G(s) + N_{f_0} H(s) + N_{eff} E(s), \tag{5-7}$$

where $G(s)$ is the $\phi(1020)$ PDF, $H(s)$ is the $f_0(980)$ PDF, $E(s)$ is the non-resonant phase space PDF (the explicit mathematical expressions for these PDFs are shown in Appendix C) and N_i are the number of events for these

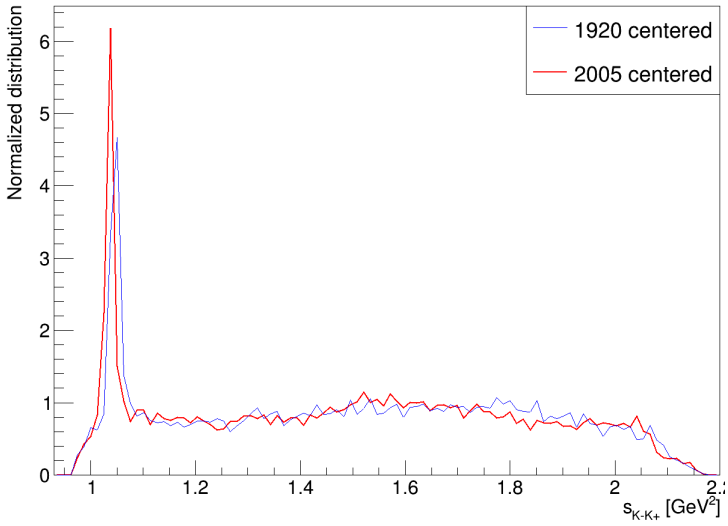

Figure 5.2: Invariant mass squared distributions for two different slices of the background region. The blue curve represents data in the region $1915 - 1925$ MeV in the invariant mass distribution while the blue curve represents the data in the region $1995 - 2010$.

components obtained from the fit. These fits are performed using the RooFit package [23]. The N_i results are used to calculate the relative fractions of the background parametrization components:

$$f_\phi = \frac{2N_\phi}{2N_\phi + 2N_{f_0} + N_{eff}}, \quad f_{f_0} = \frac{2N_{f_0}}{2N_\phi + 2N_{f_0} + N_{eff}}, \quad f_{eff} = \frac{N_{eff}}{2N_\phi + 2N_{f_0} + N_{eff}}, \tag{5-8}$$

the factor of 2 comes from the fact that we use both s_{12} and s_{13} so there will be an extra contribution to the resonances' fractions in the "combinatorial" (outside the peak) part of the background distribution. An example of these fits is shown in Fig.5.3 where the background slice used is 1930-1940 [MeV]. In total, we performed fits in six slices of the background region, each of them was 10 MeV wide.

Later, a mean of the obtained fractions in all the slices is calculated and these mean values are used to construct the final 2D background histogram as an incoherent sum of the background parametrization components. The results obtained for the fits in the different slices of the background region are shown in Table 5.1.

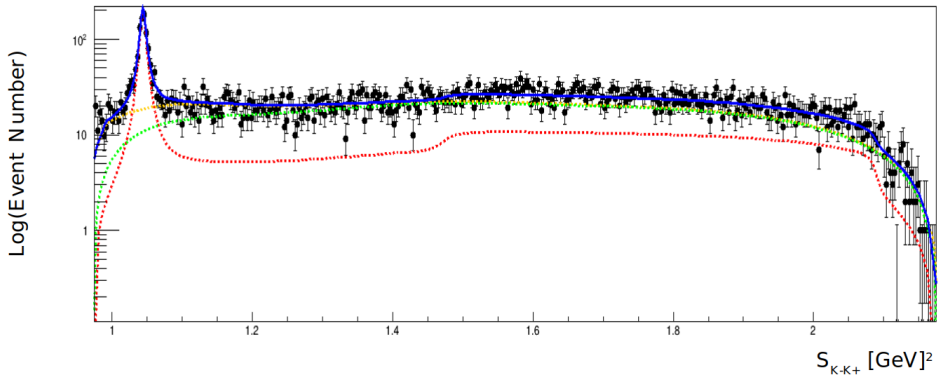

Figure 5.3: Parametrization of the $s_{K^-K^+}$ corresponding to the background region slice 1930-1940 [MeV] of the invariant mass distribution. The blue line represents the combined model with the three components: the green line represents the non-resonant phase space, the yellow line represents the parametrization of the f0(980) resonant and the red line represents the phi(1020) parametrization. This is log plot so that the contributions for each resonance are visible.

Region	f_ϕ	f_{f_00}
1915-1925	0.219	0.569
1930-1940	0.206	0.584
1945-1955	0.254	0.629
1985-1995	0.242	0.646
2000-2010	0.238	0.595
2015-2025	0.231	0.589

Table 5.1: Values obtained for the fractions of the different components of the background parametrization in the different slices of the background region

The obtained values for the fractions of the background parametrization components in the signal region of the mass spectrum are then: $f_\phi = 0.23$, $f_{f_0} = 0.60$ and $f_{eff} = 0.17$. Finally, we generated simulated samples of three-body decays using GooFit: two resonant samples of 2.3×10^5 and 6.0×10^5 events with $\phi(1020)$ and $f_0(980)$ intermediate states respectively and a non-resonant sample with 1.7×10^5 events. The 2D background histogram is constructed by plotting together all the samples (this simulates an incoherent sum). The final histogram sample contains 1M events; after plotting the histogram, we perform a cubic spline in the same way it was done for the efficiency. The final background histogram is shown in Fig. 5.4.

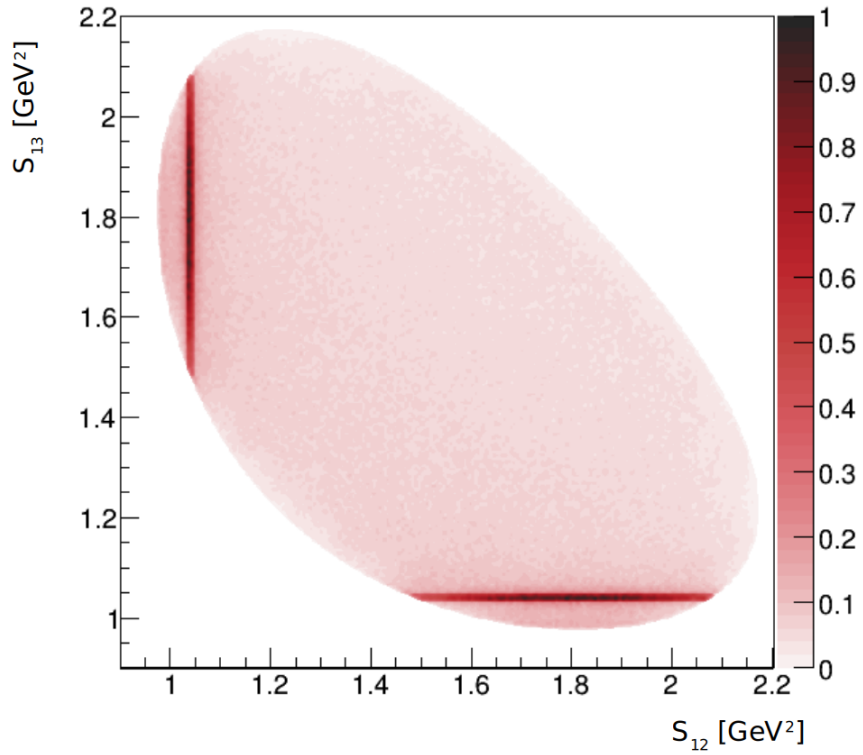

Figure 5.4: Background parametrization used in the $D_s^+ \to K^-K^+K^+$ fits.

6
Results of the $D_s^+ \to K^-K^+K^+$ amplitude analysis

In this chapter, a summary of the results obtained in the Isobar Model and the QMIPWA fits for the decay channel $D_s^+ \to K^-K^+K^+$ is presented. After the background and efficiency corrections, it was necessary to define a fitting strategy: first we identify qualitatively the resonances that are found in the phase space of this three-body decay to obtain a baseline model for the Isobar fits. In Fig. 4.7, the only resonance that can be clearly identified in the Dalitz plot is the $\phi(1020)$ because it appears as a thin line at $s_{12} \approx 1.1$ GeV^2 with its characteristic spin-1 angular distribution. Aside from this resonance, there does not exist a clear contribution from any other spin 1 resonance (possibly there exists a small contribution from $\rho(1450)$ but the low statistics in the high mass region do not allow a clear identification of this resonance). In the case of scalar resonant states, a contribution from $f_0(980)$ close to the threshold of the phase-space together with a S-wave structure may be identified and maybe another S-wave at higher mass. Therefore, we chose a baseline model based on these resonances: the $\phi(1020)$ is included with fixed coefficient $c_{\phi(1020)}$ to be used as a reference for the other coefficients c_i (magnitude and phase); $f_0(980)$ is included because it is observed to be inside the phase-space of the decay and $f_0(1370)$ is also included motivated by the studies performed for the decay $D^+ \to K^-K^+K^+$ in [32] (the mass and width of this resonance are left as free paramaters in the fits). Later, we performed several fits with different variations of the baseline model that include many combinations of the resonances allowed in the decay mode $R \to K^+K^-$; the parameters used for these resonances (mass and width) are taken from PDG [29] and they are summarized in Table 6.1. The total number of events used in the fitting procedure is 103980.

6.1
Baseline Isobar model

The baseline model is based on the model presented in the amplitude analysis of the decay $D^+ \to K^-K^+K^+$ [32]. In this model the parameters of the $\phi(1020)$ and $f_0(980)$ are fixed while the parameters of the $f_0(1370)$ (mass and width, additionally to the coefficient $c_{f_0(1370)}$) are set as floating

Resonance	**Spin**	**Lineshape**	m(MeV/c^2)	Γ(MeV/c^2)
$a_0(1450)$	0	RBW	1474	265
$f_0(980)$	0	Flatté	990	70
$f_0(1370)$	0	RBW	1370	350
$f_0(1500)$	0	RBW	1505	109
$\phi(1020)$	1	RBW	1019.461	4.266
$\rho(1450)$	1	RBW	1465	400
$f_2(1270)$	2	RBW	1275.1	185.1
$f_2'(1525)$	2	RBW	1525	73

Table 6.1: List of resonances included in the $D_s^+ \to K^-K^+K^+$ fit models along with their properties. RBW stands for Relativistic Breit-Wigner.

Resonance	**Amplitude**	**Phase** (rad)	**Fit fraction (FF)** (%)
$\phi(1020)$	1 [fixed]	0 [fixed]	50.3
$f_0(980)$	2.35 ± 0.01	0.56 ± 0.01	58.7
$f_0(1370)$	0.44 ± 0.02	-0.58 ± 0.04	4.0
			$\sum FF = 113.0$ %
			FCN = **-122657**
			$m_{f_0(1370)} = 1.401 \pm 0.001$ GeV/c^2
			$\Gamma_{f_0(1370)} = 0.073 \pm 0.002$ GeV/c^2

Table 6.2: Coefficients and fit fractions of the baseline model using the Isobar Model. Model used as a first parametrization for the phase space of the decay $D_s^+ \to K^-K^+K^+$ motivated by the studies in [32]. Uncertainties are only statistical

in the fitting algorithm. Both the $\phi(1020)$ and $f_0(1370)$ are parametrized by a RBW lineshape and the $f_0(980)$ is parametrized by a Flatté distribution. The results obtained for this model are shown in Table 6.2 and the FCN obtained is -122657. In this model, the fit cannot be resolved in the s_{K-K+} distribution at low mass (an extra peak beside the main $\phi(1020)$ peak appears) and in the s_{K+K+} distribution at high mass as shown in Fig. 6.1 (due to the high contribution of $\phi(1020)$, the region outside the peak cannot be clearly appreciated qualitatively in the invariant mass squared distributions, therefore we plot the $s_{K^-K^+}$ distribution in log scale). Given these results, it is clear that other contributions have to be included to resolve the fit in these regions. Contributions from scalar and spin 2 resonances are considered in the baseline model variations.

The invariant mass squared distributions for the baseline model are shown in Fig. 6.1 where it is clear that the model does not satisfactorily describe the data at high masses.

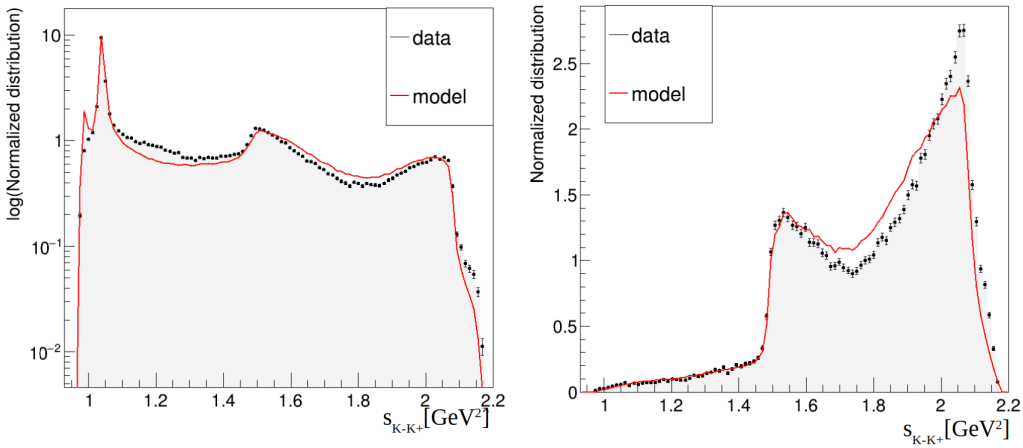

Figure 6.1: Invariant mass squared projections for the baseline model. The graph on the left shows the $s_{K^-K^+}$ distribution and the plot on the right shows the $s_{K^+k^+}$ distribution. The model histogram was plotted using a simulation generated in GooFit with the parameters obtained in the Isobar Model fit.

6.2 Isobar Model variations

We tested many models which included different combinations of the allowed resonances in the decay channel $R \to K^-K^+$ (the allowed resonances with parameters are shown in Table 6.1). Since there exist no previous work on the amplitude analysis for this decay channel, we do not have any specific preference in the number and/or combination of resonances. In all the models, the resonances were parametrized by a RBW except for the $f_0(980)$ which was parametrized by a Flatté lineshape and all parameters (mass and width) for all the resonances were set to constant except for models in which the mass and width of $f_0(1370)$ were used as a fitting parameter. No other options were explored in these fits like using the parameters of the $f_0(980)$ lineshape as fitting parameters; these variations should be tested in future research. Each model was run at least three times using the fitting algorithm to test the stability of the fit. When choosing the best models we looked at the lowest FCN with small values for the sum of the fitting fractions (to avoid big and probably unphysical interference between the resonances) and values of the mass and width of the $f_0(1370)$ resonance within an acceptable range. In general, many of the features of the phase-space could not be parametrized satisfactorily by the tested models, likely due to the limitations of the Isobar Model or the choice of lineshapes. This can be clearly appreciated in the high-mass region of the s_{K+K+} distributions, where the fits cannot resolve the final peak close to the region $s_{K+K+} \approx 2.1$ GeV^2. Also, the values of $m_{f_0(1370)}$ and $\Gamma_{f_0(1370)}$ lie within

an acceptable range but not sufficiently close to the measured values by PDG. Attempts were made to keep the limits of these parameters within the values given by PDG ($1.2 < m_{f_0(1370)} < 1.5$ [GeV] and $0.2 < \Gamma_{f_0(1370)} < 0.5$[GeV] [29]) but the obtained values reached the lower limit in most of the cases. Therefore, the limits were adjusted to: ($1.1 < m_{f_0(1370)} < 1.7$ [GeV] and $0.05 < \Gamma_{f_0(1370)} < 0.7$[GeV]. The results for the best three Isobar model fits are summarized in Table 6.3.

It is important to note that the models with lowest FCN include at least three contributions to the S-wave (the 2 resonances from the baseline model and an extra contribution). Model 1 includes, aside from the baseline model resonances, one scalar contribution $a_0(1450)$ and the two spin 2 resonances allowed in this decay channel. Model 2 has the same resonances as Model 1 with an extra contribution from $\rho(1450)$. Finally, Model 3 includes the scalar $f_0(1500)$ into Model 1. Several variations of these models were tested, however, they did not meet the requirements of a small value for the sum of the fitting fractions and a low FCN.

From Table. 6.3, we can extract some common features from the results of these models. The fraction of $\phi(1020)$ sligthly changes in the three models mantaining a value between 48%-49%. This is also a common feature of all the tested models, the value of this fraction lies within the range 45%-52% which means that the decay is dominated by the contribution from the $\phi(1020)$ but it is also dominated by a S-wave structure. In the three models, the fit fraction of $f_0(1370)$ is the largest meaning that it dominates the decay S-wave but also the $a_0(1450)$ resonance may have an important contribution. In general, all the fitting models have large contributions from S-wave components (mainly $f_0(1370)$ and $a_0(1450)$ but sometimes $f_0(1500)$) to the fitting fractions while the contributions of the spin-2 resonances stay low (about 5%).

Another interesting feature are similarity of the values obtained for $m_{f_0(1370)}$ and $\Gamma_{f_0(1370)}$. This may imply a contribution from a scalar with Γ within the range 0.25-0.29 GeV and low mass. However, the proximity of $m_{f_0(1370)}$ to $m_{f_0(980)}$ might reveal a possible effective parametrization of the S-wave at low invariant mass squared performed by the fitting algorithm. This means that the fitting algorithm has difficulty to separate the lineshapes at low mass so it might use the $f_0(1370)$ to account for the features that are not resolved by $f_0(980)$.

The invariant squared mass distributions for these three models are shown in Fig. 6.2. The solutions present small variation among themselves, therefore no conclusions about the best model out of this three might be formulated based on these distributions. In the three models, the final peak

in the $s_{K^+K^+}$ cannot be resolved by the fit, which is also a common feature among all the tested models.

Comments on the results for the Isobar Model

- In all the models tested, the fit fraction of $\phi(1020)$ lies within the range $0.42 - 0.51$, being ~ 0.48 the most common result. The values of the other fit fractions fluctuate in a inconsistent manner depending on the resonances included. However, the S-wave posseses always the highest contribution to the fit fractions.
- Models where the sum of fitting fractions was much larger than 200% were dicarded as solutions because they did not represent a physical solution, even though many of those had lower FCN values than the fitting models presented here.
- The models with the lowest FCN have at least 5 resonances, including the 3 resonances from the baseline.
- The FCN of fitting models with floating mass/width of $f_0(1370)$ was smaller compared to the FCN of the same models where these parameters were fixed in the fit.
- The region $1.9 < s_{K+K+} < 2.2$ [GeV^2] could never be fitted in a satisfactory way, independently of the resonances included. The final peak at about $s_{K+K+} \approx 2.1$ [GeV^2] could never be resolved by any of the fitting models.

6.3 QMIPWA model results

As mentioned in previous chapters the description of the S-wave is not well performed by the Isobar Model because of the difficulty presented when trying to separate the lineshapes. The QMIPWA was introduced as an alternative model to resolve the parametrization of the S-wave by modelling it with two parameters at each bin provided to the fitting algorithm. Several fits were performed using the QMIPWA where we tested different binning schemes as uniform and adaptive binning. Some of these binning schemes caused a high leaking of the $\phi(1020)$ resonance, therefore the binning had to be adjusted manually (adding/removing bins) from a uniform binning scheme in the mass spectrum until convergence of the S-wave was found with uncertainties smaller in at least one order of magnitude than their corresponding values and no-leaking from higher spin resonances was present (basically, we carefully removed bins with high uncertainty and bins where leaking from $\phi(1020)$

Model 1			
Resonance	**Amplitude**	**Phase** (rad)	**Fit fraction (FF)** (%)
$\phi(1020)$	1 [fixed]	0 [fixed]	48.5
$f_0(980)$	0.92 ± 0.05	0.83 ± 0.06	8.6
$f_0(1370)$	2.76 ± 0.14	1.92 ± 0.05	58.8
$a_0(1450)$	2.97 ± 0.07	0.31 ± 0.03	33.5
$f_2(1270)$	0.57 ± 0.05	3.11 ± 0.15	0.3
$f_2'(1525)$	1.36 ± 0.16	2.09 ± 0.11	0.3
			$\sum FF = 150$ %
			$m_{f_0(1370)} = 1.097 \pm 0.003$ GeV
			$\Gamma_{f_0(1370)} = 0.26 \pm 0.01$ GeV
			FCN = **-125887**
Model 2			
Resonance	**Amplitude**	**Phase** (rad)	**Fit fraction (FF)** (%)
$\phi(1020)$	1 [fixed]	0 [fixed]	49.8
$f_0(980)$	1.01 ± 0.05	0.43 ± 0.08	10.7
$f_0(1370)$	2.61 ± 0.11	2.13 ± 0.03	69.5
$a_0(1450)$	2.73 ± 0.08	0.37 ± 0.03	29.3
$\rho(1450)$	1.03 ± 0.14	-1.28 ± 0.03	0.7
$f_2(1270)$	0.88 ± 0.08	3.11 ± 0.06	0.8
$f_2'(1525)$	0.93 ± 0.13	1.30 ± 0.25	0.1
			$\sum FF = 161$ %
			$m_{f_0(1370)} = 1.088 \pm 0.003$ GeV
			$\Gamma_{f_0(1370)} = 0.21 \pm 0.01$ GeV
			FCN = **-125911**
Model 3			
Resonance	**Amplitude**	**Phase** (rad)	**Fit fraction (FF)** (%)
$\phi(1020)$	1 [fixed]	0 [fixed]	48.6
$f_0(980)$	1.02 ± 0.04	0.65 ± 0.06	10.7
$f_0(1370)$	2.51 ± 0.13	2.23 ± 0.07	53.8
$f_0(1500)$	0.95 ± 0.17	0.45 ± 0.13	4.5
$a_0(1450)$	1.98 ± 0.21	0.75 ± 0.13	15.0
$f_2(1270)$	0.63 ± 0.07	2.89 ± 0.11	0.4
$f_2'(1525)$	1.38 ± 0.16	0.22 ± 0.11	0.3
			$\sum FF = 133$ %
			$m_{f_0(1370)} = 1.112 \pm 0.004$ GeV
			$\Gamma_{f_0(1370)} = 0.252 \pm 0.009$ GeV
			FCN = **-125903**

Table 6.3: Coefficients, fit fractions and parameters of the $f_0(1370)$ resonance obtained for the best three Isobar Model fits. Uncertainties are only statistical

was found and added more bins in regions of high uncertainty to reduce the uncertainty of the neighbours; this process had to be done carefully because in some cases the exclusion of a single bin changed the behavior of the S-wave or caused the non-convergence of the fitting algorithm).

The fits performed initially included only the $\phi(1020)$ and the S-wave parametrization. The S-wave and the invariant mass squared distributions for the fitting model with the lowest FCN are shown in Fig. 6.3; the FCN value for this model is -125320. As shown in Fig. 6.3, the fit cannot resolve the fit in the region $s_{K^+K^+} > 1.4$ GeV^2 and the parametrization of the S-wave has high uncertainty in the region $m_{K^-K^+} > 1.24$ GeV (in general the fits using this model presented high uncertainties in this mass region regardless of the binning schemes used). Although the region $m_{K^-K^+} > 1.38$ GeV was partially solved by the binning used, the region $1.24 < m_{K^-K^+} < 1.38$ GeV still presented high uncertainties and a dicontinuity in the phase. In order to solve this issue, two methods are implemented: including more high spin resonances in the fitting model and performing the fit in the region that does not include the discontinuity in the phase.

In total, there exists 7 possible fitting models in the QMIPWA formalism that include all combinations of the allowed high spin resonances. Fits using these models were performed with the same binning scheme for all of them. The models are shown in Table 6.4 and the S-wave parametrization for each model is shown in Fig. 6.4. The QMIPWA fitting model that includes the resonances $\phi(1020)$ and $f_2(1270)$ did not converge so a parametrization for the S-wave is not provided.

From Table 6.4 and Fig. 6.4, we can identify different features: firstly, the FCN of the QMIPWA is smaller than the FCN values obtained using the Isobar Model by 100 units approximately. Also, looking at the S-wave amplitude and phase distributions, it can be appreciated that all models present a discontinuity in the phase distribution at about $m_{K^-K^+} \approx 1.24$ GeV. In the models where the $\rho(1450)$ resonance is included, this discontinuity is more explicit; additionally to this, a new peak appears at about $m_{K^-K^+} \approx 1.24$ GeV in these fits. Also the models c and f with only spin 2 resonances aside from $\phi(1020)$ have a similar distribution as the baseline model with only $\phi(1020)$. This is expected from the Isobar Model fits because the spin 2 reonances have a minimal contribution to the phase-space of the decay.

Unfortunately, the first strategy did not provide a resolution to the discontinuity in the phase distribution of the S-wave. Therefore, a plot of a subregion of the mass spectrum is performed with model "g" (this model was chosen because it has the lowest FCN value). The first attempt to fit

Model	$\phi(1020)$	$\rho(1450)$	$f_2(1270)$	$f_2'(1525)$	**FCN**	$\sum FF$
a	✓	✓			-126082	181
b	✓		✓		no convergence	-
c	✓			✓	-125620	89
d	✓	✓	✓		-126063	202
e	✓	✓		✓	-126216	213
f	✓		✓	✓	-125642	94
g	✓	✓	✓	✓	-126292	223

Table 6.4: Models tested using the QMIPWA formalism.

the data until $m_{K^-K^+} \approx 1.24$ GeV was not succesfully completed because of the non-convergence of the fitting algorithm so the range was increased to $m_{K^-K^+} \approx 1.34$ GeV. The fit was run with different binning schemes and two solutions in particular presented different modeling of the S-wave, these distributions are shown in Fig. 6.5. The fact that two different solutions are found with two different binning schemes demonstrates the limitations of the QMIPWA to parametrize the S-wave and a possible inability to represent the S-wave using the QMIPWA.

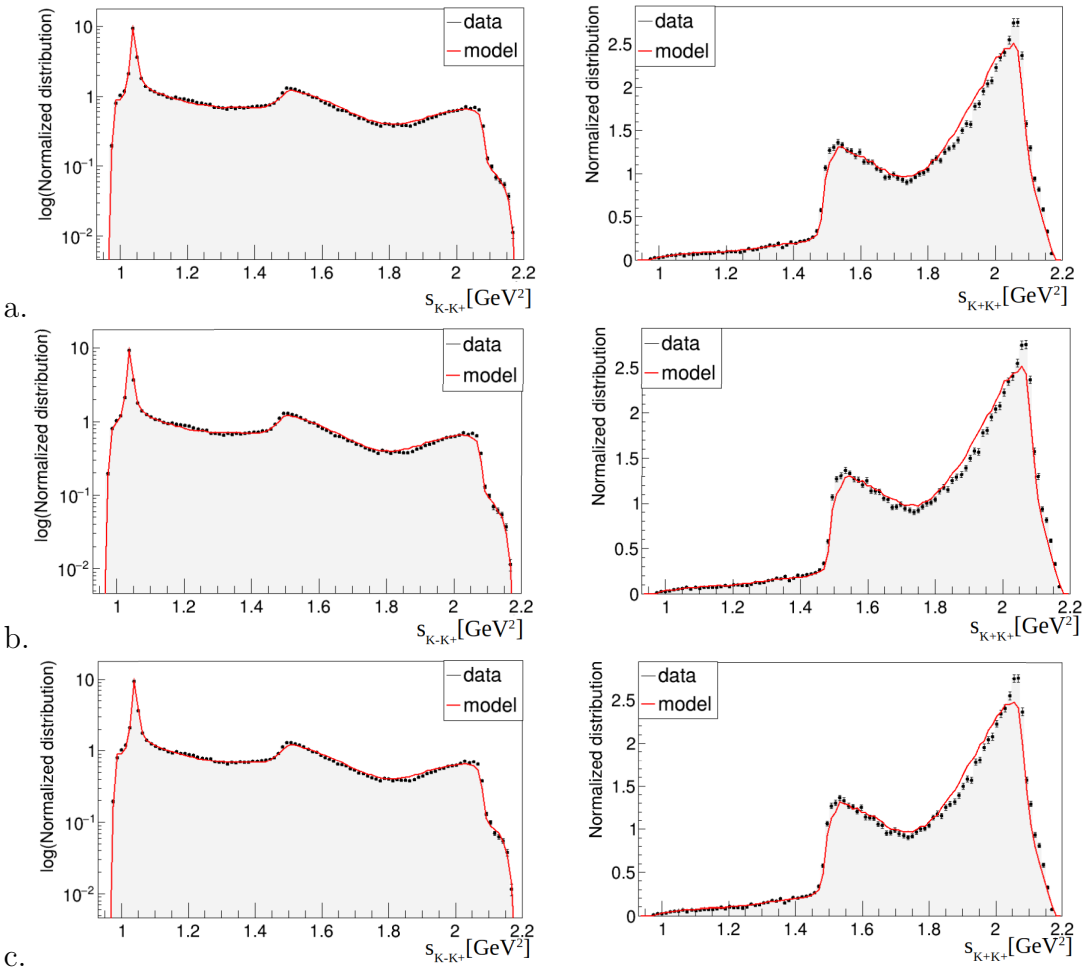

Figure 6.2: Invariant mass squared distributions for the Isobar model fits 1, 2 and 3 (a, b and c respectively). On the left, the $s_{K^-K^+}$ projection is shown and the $s_{K^+K^+}$ projection is shown on the right. The red line represents the fitting model while the black points represent the data. The model histogram was plotted using a sample generated in GooFit with 1M events.

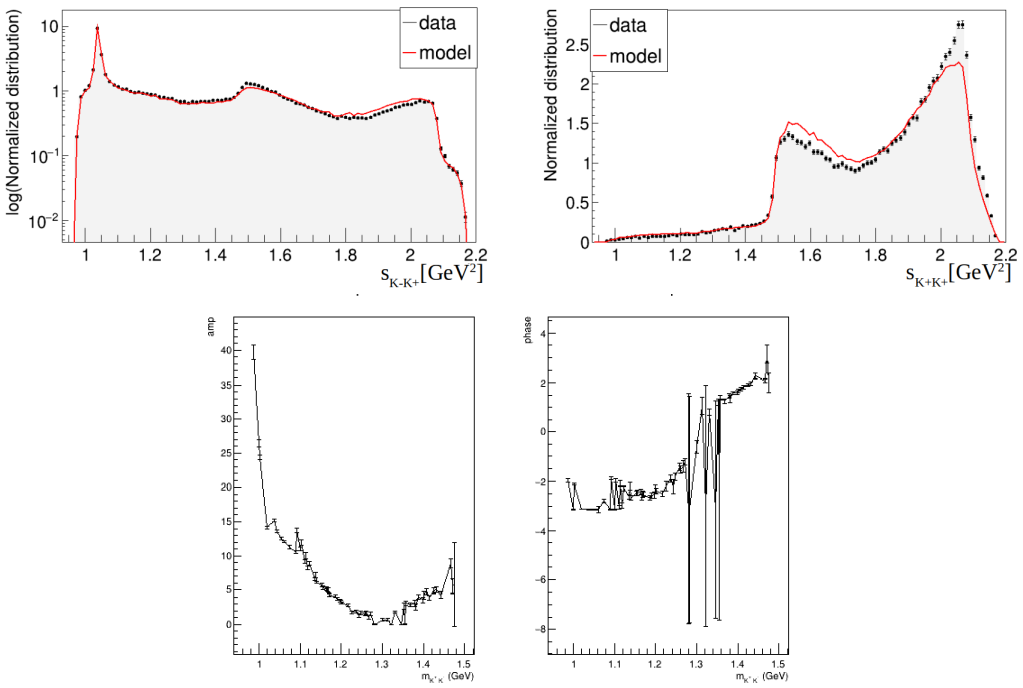

Figure 6.3: Invariant mass squared distributions and S-wave parametrization obtained in the QMIPWA fit with only $\phi(1020)$ as a high spin resonance. The left-hand side of the bottom figure shows the amplitude a_i of the parametrized S-wave and the phase ϕ_i of the S-wave is shown on the right hand side of the bottom figure. The interpolation is performed by a cubic spline. Number of bins provided to model the S-wave was 76. The $s_{K^-K^+}$ distribution is shown in the top figure left and the $s_{K^+K^+}$ distribution is shown in the top figure right.

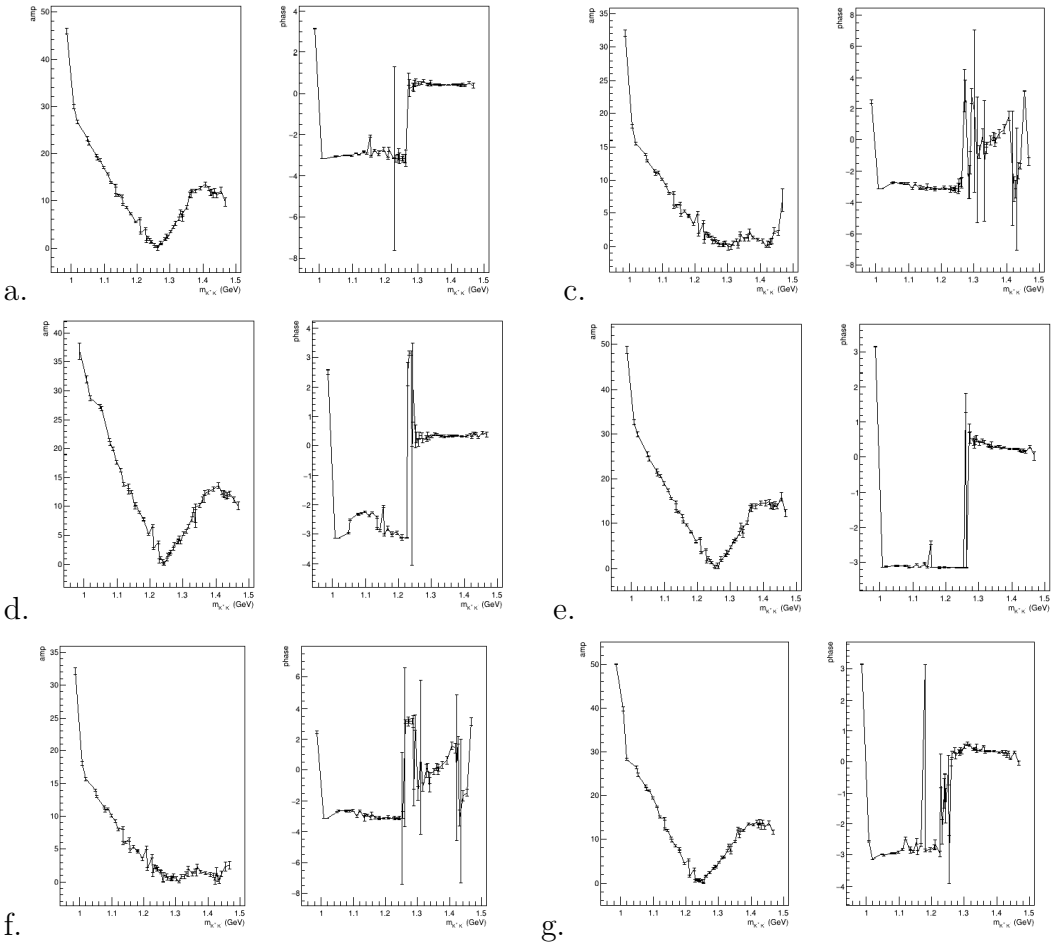

Figure 6.4: Amplitudes and phases of the S-wave parametrizations for the allowed fitting QMIPWA models. The fitting algorithm converged only for 6 models given in Table 6.4. The amplitude distributions are shown on the left-hand side of the figures and the phases on the right hand-side. The number of bins used to fit the S-wave was 65. The invariant squared mass distributions are shown in Fig. D.1 in Appendix D.

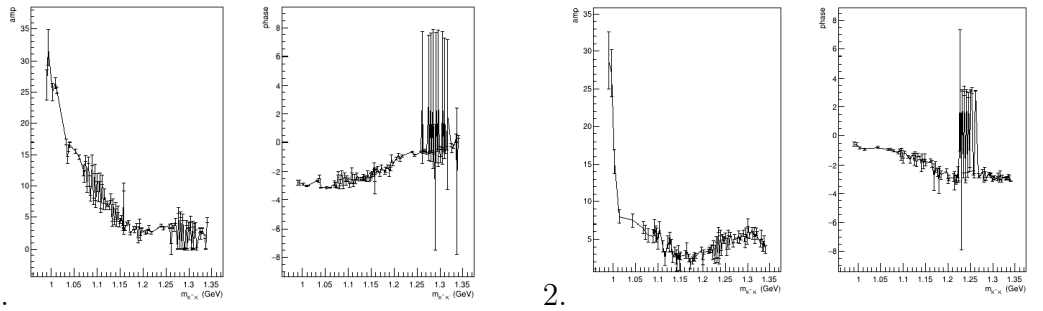

Figure 6.5: Amplitudes and phases of the S-wave parametrizations for model "g" with two different binning schemes. 1. is fitted with 78 bins while 2. is fitted using 64 bins. The removed bins correspond to the high uncertainty region in the phase distribution. The amplitude distributions are shown on the left-hand side of the figures and the phases on the right hand-side.

7
Conclusion

In this dissertation, we have performed an amplitude analysis of the decay $D_s \to K^-K^+K^+$ using the Run 2 data from the LHCb experiment. The final data set after selection included 103980 events. The data selection after trigger was mostly performed by Carolina Bolognani in [27], only the final BDT requirement was increased so a 90% purity was achieved in the sample. A parametrization of the detection efficiency was performed including a study of the data/MC differences and also a background parametrization was performed. Two phenomenological models were employed in the fitting procedure: the Isobar Model and the QMIPWA. Initially, we chose a baseline for the Isobar Model fit where three resonances appear in the phase-space: $\phi(1020)$, $f_0(980)$ and $f_0(1370)$ where the parameters (mass and width) of the $f_0(1370)$ were set as floating in the fitting algorithm. This fitting model is motivated by the work done in [32].

The baseline model shows the need of a different parametrization since the fit cannot resolve several features of the data distribution especially in the high $s_{K^+K^+}$ region, this is clearly appreciated in Fig. 6.1 where the fit is not resolved by any of the models in this region. Several fits were performed with different combinations of the allowed resonant states in the decay mode $R \to K^-K^+$; all of them including the baseline chosen for the Isobar Model fits. Then, we chose the three fitting models with the smallest value of FCN where the sum of the fit fractions lies below 200%, because high values for the sum do not represent physically allowed parametrizations. The results for the three best fits are shown in Table 6.2 where the highest contribution to the fit fractions comes from $f_0(1370)$ and $\phi(1020)$. This is expected as seen in Fig. 4.7 where a thin line coming from $\phi(1020)$ and a S-wave distribution are clearly present in the phase-space. These results show a qualitative description of the phase-space of the decay $D_s^+ \to K^-K^+K^+$ but they should be carefully analyzed in future research since an acceptable fit with reliable results could not be found; especially because the best models could not resolve the fit in the region $s_{K^+K^+} > 1.8$ GeV^2 (and in general any of the proposed models could resolve the fit in this region) likely due to the lack of resonant interference in that region: the Isobar Model uses a reference to measure the relative phase of

the resonances and without any high-spin resonance in the high mass region, the algorithm cannot find a good parametrization.

Despite of the fact that a satisfactory fit was not obtained, some features of the phase-space can be extracted from these results. First, given that the phase space is dominated by the $\phi(1020)$ resonance and the S-wave, contributions from spin 2 resonances are small. This is reflected in the values for the fit fractions of the $f_2(1270)$ and the $f_2(1525)$ which always lie in the range 0.2-0.8%. This is physically expected because the $f_2(1270)$ resonance decays primarily in the $\pi^-\pi^+$ decay mode and also the peak of $f_2(1525)$ is outside the phase space of the decay of the decay $D_s^+ \to K^-K^+K^+$ so a small contribution of these resonances should be present in Dalitz plot. Also, it is important to note that the inclusion of more resonances reduces the value of the FCN in the fits (as expected, because the FCN value decreases with the number of parameters given to the fitting algorithm) but not many of these solutions represent physically allowed states given that the sum of the fitting fractions is extremely large.

Another feature that can be extracted from these results is the apparent complexity of the S-wave. The results presented with the lowest FCN values include at least 3 scalar resonant states and in general the fits that better modelled the invariant masses squared distributions include at least 5 resonant states. Apparently, the structure of the S-wave cannot be modelled by the lineshapes used or the choice of parameters, therefore, further studies with different settings should be attempted (change lineshapes, mass, widths of the scalar resonances). It is also possible that the Isobar Model itself might not able to parametrized the S-wave in this decay mode so other phenomenological models should be implemented.

In the three best Isobar fitting models, the values for $\Gamma_{f_0(1370)}$ are compatible suggesting that this value should be the accurate width value of this resonant state. However, this fact should be carefully analyzed given that the masses lie within a similar range among themselves but they are not compatible.

Also, the fit fraction values of the $\phi(1020)$ for all the models tested lie within the range 40%-53%, results that are expected to be found in further studies. In the case of the scalar resonances, these values fluctuated inconsistently depending on the resonances included in the fitting models. This demonstrates the complexity of the S-wave and the inability of the Isobar Model to decribe this S-wave.

In the QMIPWA fitting results, we can appreciate that the S-wave in fact posseses a complicated structure that could not be resolved by this formalism.

The fitting models do not model the invariant mass squared distributions satisfactorily. Apparently the QMIPWA is not well suited to describe this decay channel likely due to the absence of other high spin resonant states in the high mass region to be used as a reference. Another interesting feature is the discontinuity of the S-wave phase distribution at about $\phi = 1.26$ rad that becomes more prominent when $\rho(1450)$ is included in the fit. This discontinuity may arise from the lack of interference in the region $m_{K^+K^-} > 1.24$ GeV so that the fitting algorithm will not provide a physical solution, however this result should be further analyzed. Another possible explanation is that the fitting algorithm produces an artificial interference between the $\rho(1450)$ and the S-wave to account for the lack of data points in the high mass region. The inability of the QMIWA to model the data becomes more clear when comparing the Isobar Model 1 and the QMIPWA Model f; they are compatible models and it is expected to find a lower FCN value for model f of because it has more parameters, which is not the case.

In Fig. 7.1, the S-wave parametrizations for three best fitting models using the Isobar Model are shown. The S-wave differs significantly among all of these models so the results do not provide a conclusion about the structure of the S-wave in the phase-space of the $D_s^+ \to K^-K^+K^+$ decay. In addition, the fits performed in sub-regions of the phase space demonstrate more clearly the strange behavior of the S-wave phase distribution: the fact that two different solutions are obtained using only different binning schemes with the same fitting model might reflect the impossibility of using the QMIPWA to describe the decay channel $D_s^+ \to K^-K^+K^+$.

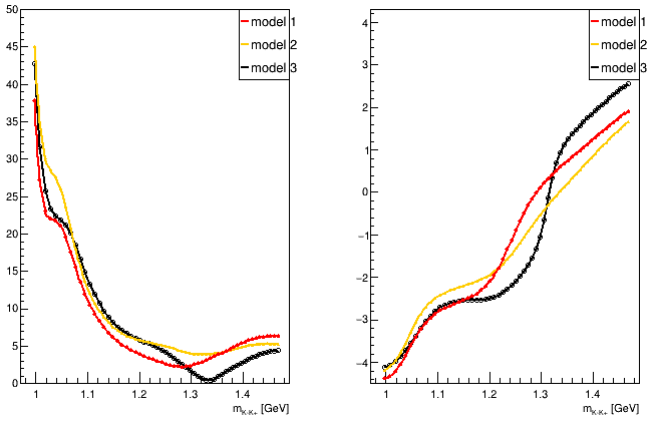

Figure 7.1: Amplitude and phase of the S-wave parametrization obtained for each one of the best Isobar Model fits. On the left hand side of the figure, the amplitude of the S-wave is shown. The phase is shown on the right-hand side.

Since the QMIPWA is a quasi-model independent, the results obtained

for the coefficients are not expected to vary by a significant amount (this because the high-spin resonances used are supposed to be well accounted by the Isobar Model). However, when comparing the S-wave obtained for the best results of the fitting using the Isobar Model (shown in Fig. 7.1) and the S-wave obtained by the QMIPWA (shown in Fig. 6.3), a great variation is clearly noted. Both phenomenological models may have found two different mathematical possible solutions, which might not have a physical meaning. Therefore, we are not able to provide a conclusion for the $D_s^+ \to K^-K^+K^+$ decay parametrization.

This is the first time that an amplitude analysis of the $D_s^+ \to K^-K^+K^+$ decay is performed with a sample of about 100 k events. The main qualitative features of the resonant structure were obtained, however, a full quantitative description was not achieved due to the limitations of the phenomenological models. Further phenomelogical approaches are needed as well as larger data samples (to be collected in the LHCb Run 3) to attempt to obtain an acceptable quantitative description of this decay channel.

Bibliography

[1] EVANS, L.; BRYANT, P.. **LHC machine**. Journal of Instrumentation, 3(08):S08001–S08001, aug 2008.

[2] ALTARELLI, G.. **The Standard Model of Particle Physics**. arXiv preprint hep-ph/0510281, 2005.

[3] THOMSON, M.. **Modern Particle Physics**. Cambridge University Press, New York, 2013.

[4] KIBBLE, T. W.. **The Standard Model of Particle Physics**. European Review, 23(1):36–44, 2015.

[6] BYCKLING, E.; KAJANTIE, K.. **Particle Kinematics**. A Wiley-Interscience publication. Wiley, 1973.

[7] BACK, J.; OTHERS. **Laura ++: A Dalitz Plot Fitter**. Computer Physics Communications, 231:198–242, 2018.

[8] PETKOV, V.; ZWORSKI, M.. **Breit–Wigner Approximation and the Distribution of Resonances**. Communications in Mathematical Physics, 204:329–351, 1999.

[9] ZEMACH, C.. **Use of Angular-Momentum Tensors**. Phys. Rev., 140:B97–B108, Oct 1965.

[10] BLATT, J.; WEISSKOPF, V.. **Theoretical Nuclear Physics.** Wiley & Sons Inc., New York, 1952.

[11] BOHM, A. R.; SATO, Y.. **Relativistic Resonances: Their masses, widths, lifetimes, superposition, and causal evolution**. Phys. Rev. D, 71:085018, Apr 2005.

[12] BARU, V.; HAIDENBAUER, J.; HANHART, C.; KUDRYAVTSEV, A. ; MEISSNER, U.-G.. **Flatté-like distributions and the a0(980)/f0(980) mesons**. The European Physical Journal A, 23(3):523–533, jan 2005.

[13] ABLIKIM, M.; OTHERS. **Resonances in J / $\psi \to \phi\pi^+\pi^-$ and ϕK^+K^-**. Phys. Lett. B, 607:243–253, 2005.

[14] ANDREASSEN, R.; OTHERS. **GooFit: A library for massively parallelising maximum-likelihood fits**. J. Phys. Conf. Ser., 513:052003, 2014.

[15] **ROOT master - Reference Guide**. `https://root.cern/doc/master/classRooStats_1_1SPlot.html`, 2008. [software, v.2.91]. Accessed: 2022-11-05.

[16] PICH, A.. **The Standard Model of Electroweak Interactions**. In: 2010 European School of High Energy Physics, p. 1–50, 2012.

[17] WORKMAN, R. L.; OTHERS. **Review of Particle Physics**. PTEP, 2022:083C01, 2022.

[18] WOLFENSTEIN, L.. **Parametrization of the Kobayashi-Maskawa Matrix**. Phys. Rev. Lett., 51:1945–1947, Nov 1983.

[19] ANTUNES-NOBREGA, R.; OTHERS. **LHCb technical design report: Reoptimized detector design and performance**. Technical Report CERN-LHCC-2003-030, CERN, 2003.

[20] COLLABORATION, T. L.; OTHERS. **The LHCb Detector at the LHC**. Journal of Instrumentation, 3(08):S08005, aug 2008.

[21] GASSNER, J.; LEHNER, F. ; STEINER, S.. **The mechanical Design of the LHCb Silicon Trigger Tracker**. Technical Report LHCb-2004-110, CERN-LHCb-2004-110, CERN, Geneva, 2010.

[22] AAIJ, R.; OTHERS. **LHCb Detector Performance**. International Journal of Modern Physics A, 30:1530022, 2015.

[23] VERKERKE, W.; KIRKBY, D. P.. **The RooFit toolkit for data modeling**. eConf, C0303241:MOLT007, 2003.

[24] ESHRAIM, W. I.. **Phenomenology of a pseudoscalar glueball and charmed mesons**. PhD thesis, Goethe Universität Frankfurt am Main, Frankfurt U., 2022.

[25] GARCIA, L.; HENRY, L.; KISHOR, B. ; OYANGUREN, A.. **Tracking performance for long-lived particles at LHCb**. Journal of Physics: Conference Series, 1525:012095, 04 2020.

[26] BELYAEV, I.; CARBONI, G.; HARNEW, N.; MATTEUZZI, C. ; TEUBERT, F.. **The history of LHCb**. The European Physical Journal H, 46(1), mar 2021.

[27] DA SILVA BOLOGNANI, C.. **Search for CP violation in the decays $D_s^+ \to K^-K^+K^+$ and $D+ \to K^-K^+K^+$ in the LHCb experiment**. Master's thesis, Pontificia Universidade Catolica do Rio de Janeiro, August 2021.

[28] MATHWORLD, W.. **Chebyshev Polynomial of the First Kind**. `https://mathworld.wolfram.com/ChebyshevPolynomialoftheFirstKind.html`, 2022. Accessed in: 2022-12-05.

[29] WORKMAN, R. L.; OTHERS. **Review of Particle Physics**. PTEP, 2022:083C01, 2022.

[30] AITALA, E. M.; OTHERS. **Model-independent measurement of S-wave $K^-\pi^+$ systems using $D^+ \to K\pi\pi$ decays from Fermilab E791**. Phys. Rev. D, 73:032004, 2006.

[31] LHCB COLLABORATION. **Tracking strategies used in LHCb**. `https://twiki.cern.ch/twiki/bin/view/LHCb/LHCbTrackingStrategies`, 2012. Accessed: 2023-02-01.

[32] AAIJ, R.; OTHERS. **Dalitz plot analysis of the $D^+ \to K^-K^+K^+$ decay**. Journal of High Energy Physics, 2019(4), apr 2019.

[33] HERNDON, D.; SODING, P. ; CASHMORE, R. J.. **A GENERALIZED ISOBAR MODEL FORMALISM**. Phys. Rev. D, 11:3165, 1975.

[34] GELL-MANN, M.. **A Schematic Model of Baryons and Mesons**. Phys. Lett., 8:214–215, 1964.

[35] YANG, G.; PING, J. ; SEGOVIA, J.. **Tetra- and Penta-Quark Structures in the Constituent Quark Model**. Symmetry, 12(11):1869, 2020.

[37] SJÖSTRAND, T.; MRENNA, S. ; SKANDS, P.. **A brief introduction to PYTHIA 8.1**. Computer Physics Communications, 178(11):852–867, 2008.

[38] CLEMENCIC, M.; OTHERS. **The LHCb simulation application, Gauss: Design, evolution and experience**. J. Phys. Conf. Ser., 331:032023, 2011.

[39] LANGE, D. J.. **The EvtGen particle decay simulation package**. Nucl. Instrum. Meth. A, 462:152–155, 2001.

[40] AGOSTINELLI, S.; OTHERS. **GEANT4–a simulation toolkit**. Nucl. Instrum. Meth. A, 506:250–303, 2003.

[41] ROGOZHNIKOV, A.; OTHERS. **Reweighting algorithms**. `https://arogozhnikov.github.io/hep_ml/reweight.html`, 2017. Accessed: 2023-03-05.

A
Resonant states in the $R \to K^-K^+$ two-body decay channel

There are 8 allowed resonant states in the decay channel $R \to K^-K^+$. the Dalitz plots of this resonant states are shown in Fig. A.1.

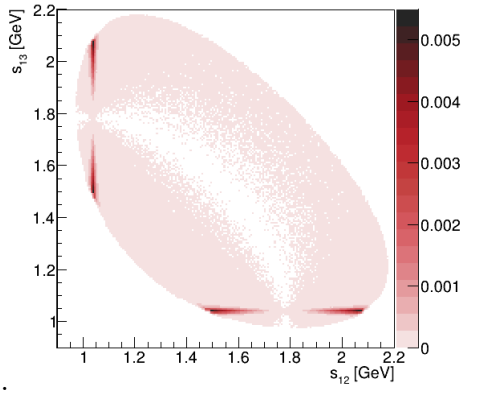

a.

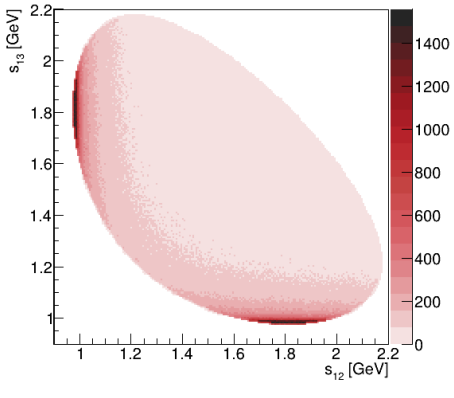

b.

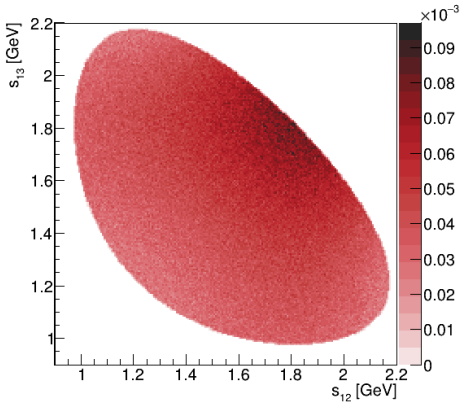

c.

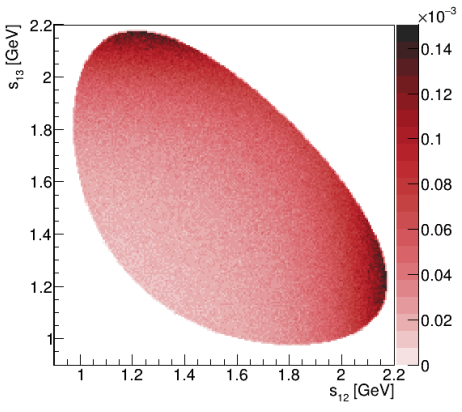

d.

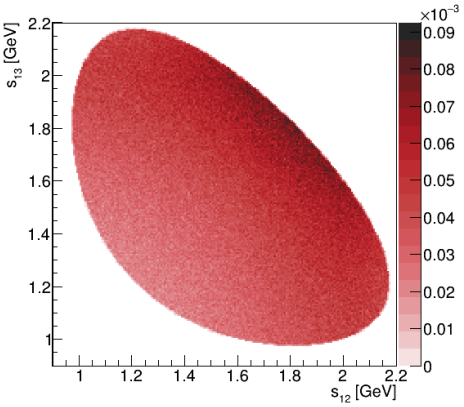

e.

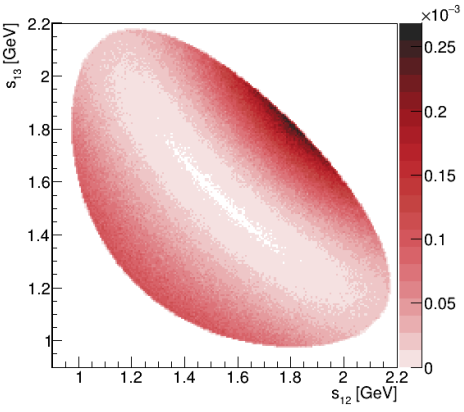

f.

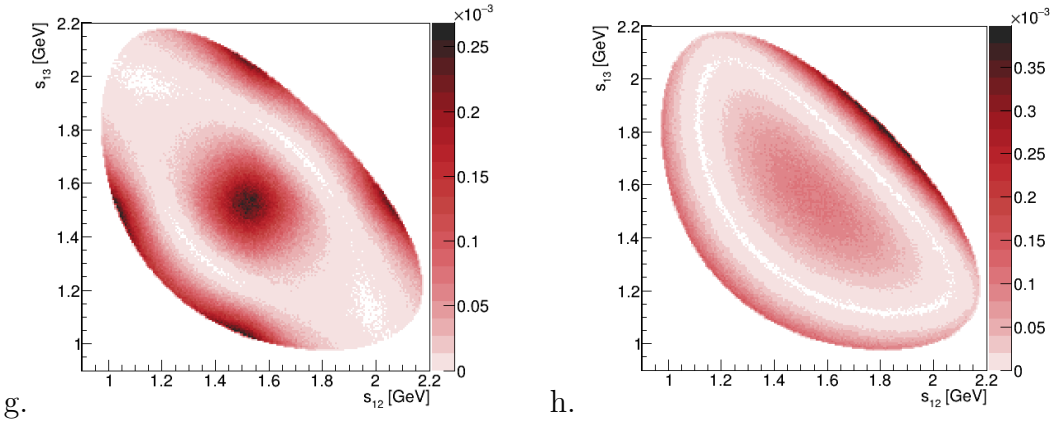

g. h.

Figure A.1: Dalitz plot of the allowed resonant states in the decay channel $D_s^+ \to K^- K^+$: a. $\phi(1020)$, b. $f_0(980)$, c.$f_0(1370)$, d. $f_0(1500)$, e. $a_0(1450)$, f. $\rho(1450)$, g. $f_2(1270)$ and h. $f_2'(1525)$

B
Resonant structure weight and reweighting

The reweighting process accounts for the differences of the data sample and the Monte Carlo simulation variables. These differences come from the fact that the MC is generated without a resonant structure. The resonant structure is implemented in the MC as a weight which is obtained from as a 2D-histogram containing only the dynamical structure of the phase space of the $D_s^+ \to K^-K^+K^+$ decay channel. The 2D-histogram for the dynamical weight is shown in the figure below.

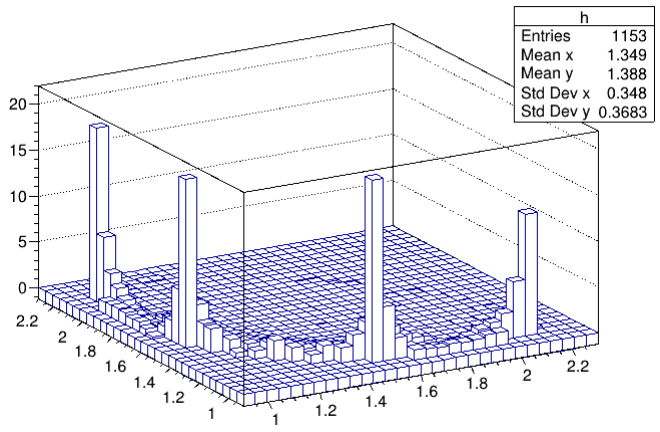

Figure B.1: Resonant struture weight histogram. It contains the resonant structure of the decay excluding the background contribution and the effects of the detection efficiency.

This resonant structure weight also provides insight about the resonant contributions in the this decay channel. The resonant structure is clearly dominated by the $\phi(1020)$ and lacks of contributions in the high mass region.

After the resonant structure correction, the reweighting algorithm is used to account for the remaining differences between the distributions of the data and the MC. The distribution of variables used in the reweighting before and after the procedure are shown in the figures below.

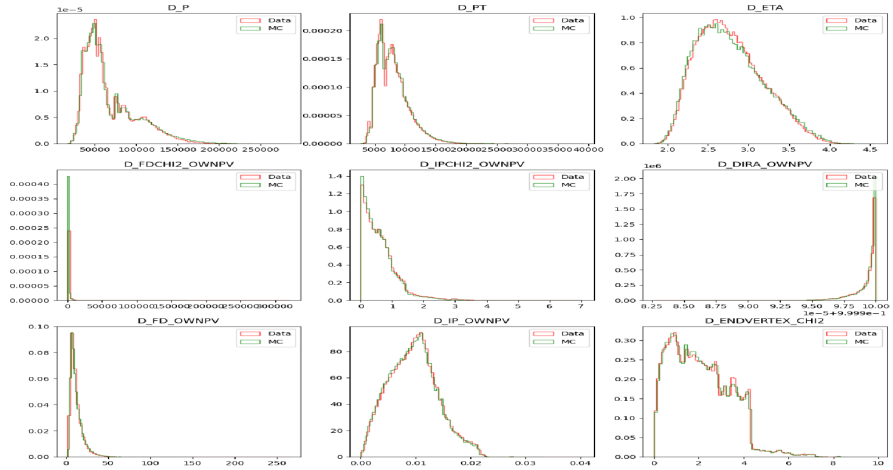

Figure B.2: Distribution of variables used in the reweighting process before the reweigthing. All histograms are normalized.

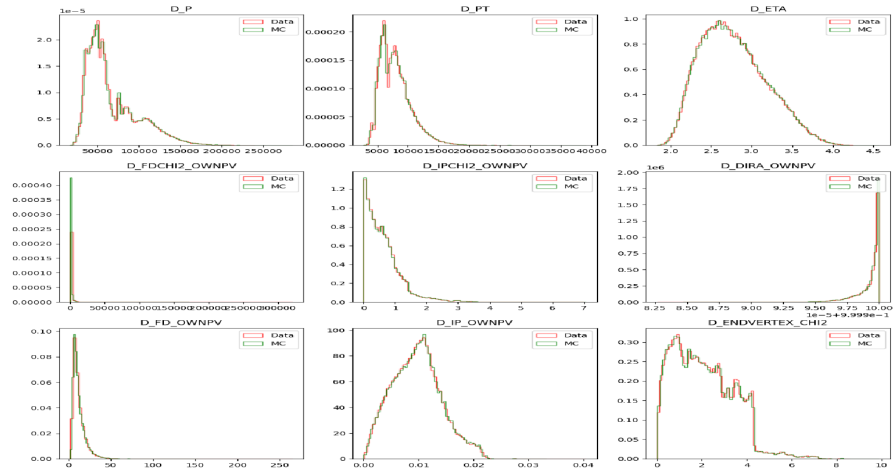

Figure B.3: Distribution of variables used in the reweighting process after the reweigthing. All histograms are normalized.

C
PDFs for the background parametrization components

The components used in the background parametrization are the resonant states that are visible in the background region of the invariant mass spectrum: $\phi(1020)$, $f_0(980)$ and the non-resonant phase space distribution. All of them include the detector efficiency effects. For this reason, a fit of the 1D efficiency has to be obtianed. This is achieved by performing a fit of the $s_{K^-K^+}$ distribution of the Monte Carlo. A suitable model found for the fit is given by the equation shown below:

$$E(s) = f_{cheb}\mathcal{C}(s) + (1 - f_{cheb})\left[f_{ps}\mathcal{P}(s) + (1 - f_{ps})\mathcal{G}\right] \tag{C-1}$$

where f_{cheb} and f_{ps} are the fractions of events related to the Chebychev distribution and to the phase-space distribution respectively, $\mathcal{C}(s)$ is a normalized fourth degree Chebychev polynomial of the first kind [28], $\mathcal{P}(s)$ is the normalized non-resonant three-body decay phase space distribution given by the expression:

$$\mathcal{P}(s) \propto \frac{\lambda^{1/2}(s, m_K^2, m_K^2)\lambda^{1/2}(m_{D_s}^2, s, m_K^2)}{s} \tag{C-2}$$

and $\mathcal{G}(s)$ is the Gamma distribution given by:

$$\mathcal{G}(s) = \frac{(s-\mu)^{\gamma-1}\exp(-(s-\mu)/\beta)}{\Gamma(\gamma)\beta^{\gamma}}. \tag{C-3}$$

The parameters obtained in the best fit with this parametrization are shown in Table C.1, similarly a plot for the best fit is shown in Fig. C.1

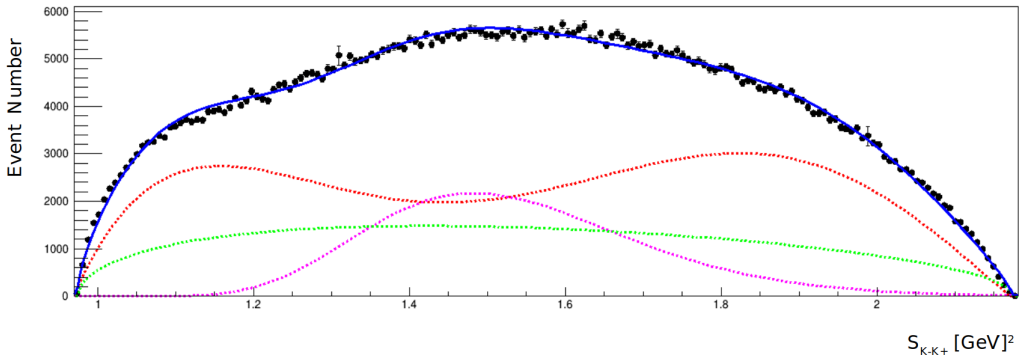

Figure C.1: Parametrization of the $s_{K^-K^+}$ distribution of the Monte Carlo phase space. The blue line represents the combined model with the three components: the green line represents the three-body decay phase space, the purple line represents the gamma function with parameters given in Table C.1 and the red line represents the Chebychev polynomial PDF.

Parameters	Value
a_0	-0.14509 ± 0.00003
a_1	-0.64758 ± 0.00502
a_2	-0.11413 ± 0.00003
a_3	-0.38182 ± 0.00004
a_4	0.20928 ± 0.00004
γ	1.026 ± 0.347
μ	0.98 ± 0.01
β	0.054 ± 0.001
f_{cheb}	0.538 ± 0.004
f_{ps}	0.602 ± 0.003

Table C.1: Parameters obtained for the $s_{K^-K^+}$ fit of the Monte Carlo. The parameters a_i are the coefficients of the Chebyshev polynomial; γ, μ and β are the parameters of the Gamma function. f_i are the relative fractions of the components of the total PDF. Uncertainties are statistical only.

The PDF's used to represent the $\phi(1020)$ and $f_0(980)$ are based on the lineshapes used to parametrize these resonances in the Isobar Model (in the case of the $\phi(1020)$ a RBW and for the $f_0(980)$ a Flatté distribution):

$$F(s) = fN_1\mathcal{D}(s)\mathcal{P}(s)E(s) + (1-f)N_2\left(\int_{s_{min}}^{s_{max}}\mathcal{D}(s')ds'\right)\times E(s) \qquad \text{(C-4)}$$

where N_1 and N_2 are normalization constants and $\mathcal{D}(s)$ is the squared of the respective lineshape. The final model used for the background parametrization is given by the following expression:

$$B(s) = N_\phi G(s) + N_{f_0} H(s) + N_{eff} E(s), \tag{C-5}$$

where N_i are the yields for each component of the background parametrization (this fit is performed using the roofit extended package which returns the estimated number of events instead of the fractions for each component of the model), $E(s)$ is the parametrization of the efficiency given in Eq. C-1 and $G(s)$, $H(s)$ are the distributions that represent the resonant phase space with $\phi(1020)$ and $f_0(980)$ respectively, shown in Eq.C-4.

D
QMIPWA invariant mass distributions

The invariant mass squared distributions obtained in the models *a* to *g* are presented in the figure below:

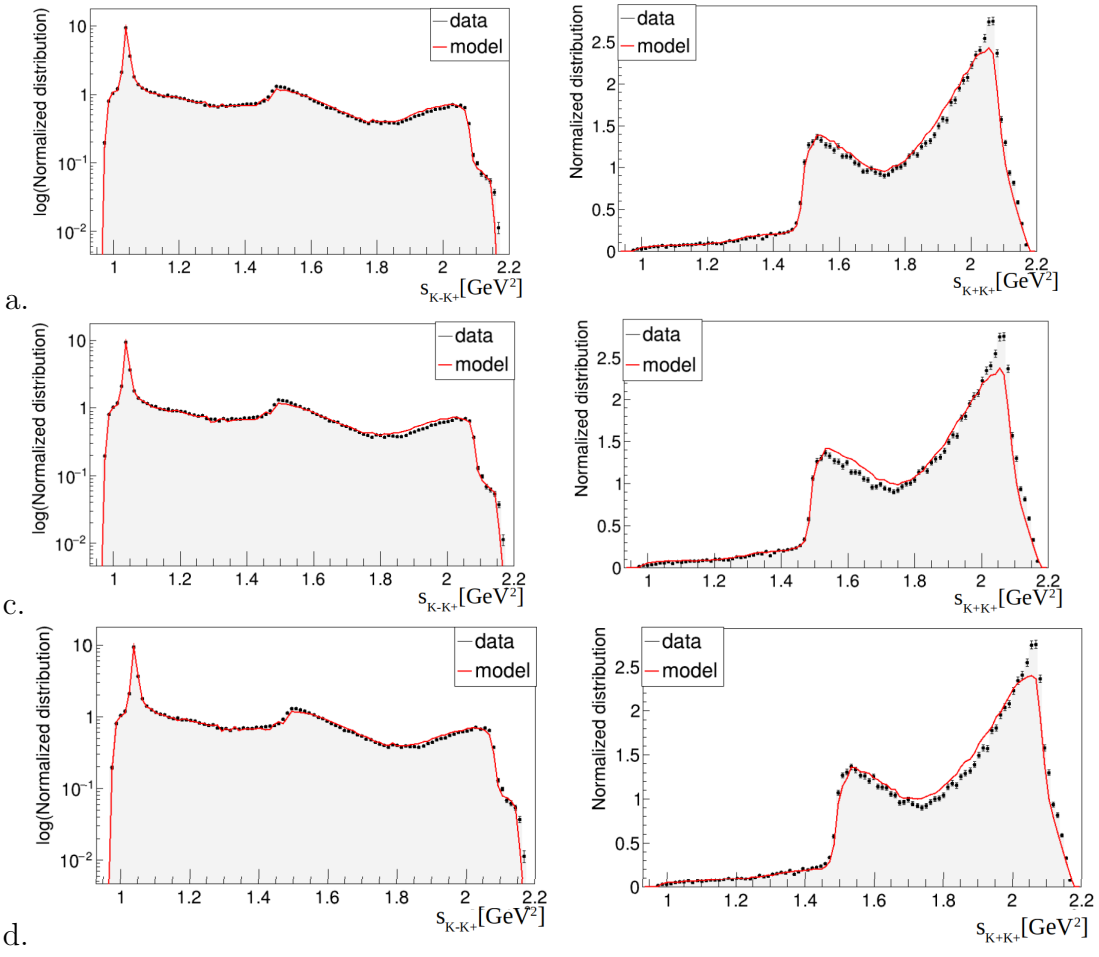

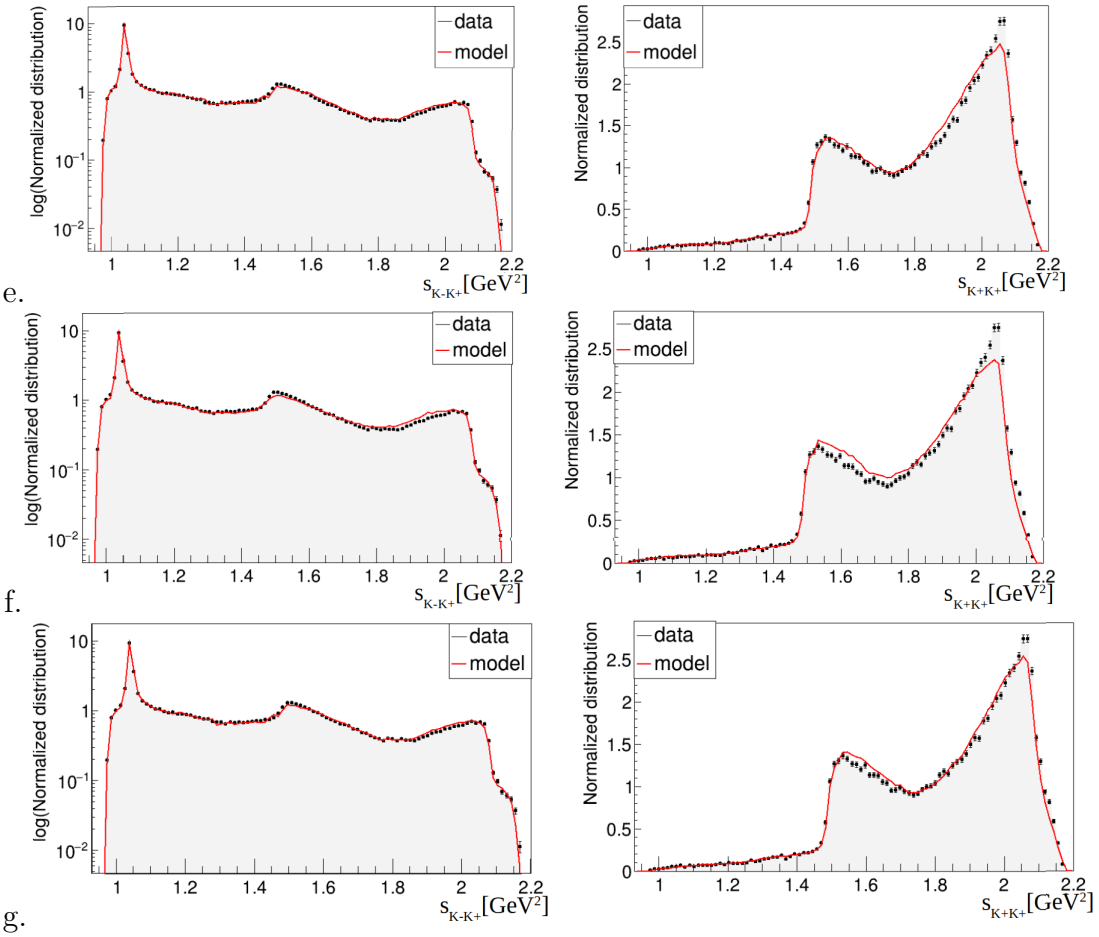

Figure D.1: Invariant mass squared distributions for Isobar model fits *a*, *c*, *d*, *e*, *f* and *g*. On the left, the $s_{K^-K^+}$ projection is shown and the the $s_{K^+k^+}$ projection is shown on the right. The red line represents the solution of the fit while the black points represent the data. The model histogram was plotted using a sample generated in GooFit with 1M events.